Dissertation

Study on Power Generating System for Dielectric Elastomers driven by Karman Vortex Street

カルマン渦列により駆動する誘電エラストマーを用いた発電システムに関する研究

Graduate School of Engineering
Yokohama National University

Kenta Hasegawa

長谷川 賢太

September 2015

ABSTRACT

While the demand for electric energy has been growing due to population increase and improvement in living standards, power generations utilizing renewable energy are in the spotlight nowadays because of their impacts to global warming and considerations of nuclear accidents and so forth. Hydropower generation is the conventional method of producing electricity from renewable energy sources. Since large-scale hydroelectricity requires the construction of dams that cause environmental damages, the development of smaller-scale hydroelectricity has recently been anticipated. Conventional electric generators using electromagnetic induction, however, may not be suitable to down-scaling. These electric generators tend to operate most efficiently in a narrow range of high frequencies. Accordingly, electricity generation systems by electric generators using electromagnetic induction include a mechanical or hydraulic transmission, resulting in more complex and larger systems.

Dielectric elastomers (DEs) are one of the most promising artificial muscles and a new transducer technology that is capable of converting mechanical energy into electrical energy. Compared to conventional power generators using electromagnetic induction or piezoelectric effect, generators using dielectric elastomers have high energy density and can efficiently produce electricity at low frequency.

In this study, we proposed a small-scale power generating system for dielectric elastomers driven by Karman vortex street which are present in the wake of a cylinder. This system extracts mechanical energy from fluid energy using the vibration of a wing which is set in the Karman vortex street in response to hydrodynamic force. The mechanical energy is transmitted to a DE generator through a shaft and subsequently converted into electrical energy. In order to investigate the power generating performance and feasibility of the proposed system, the experimental model was fabricated and tested in a small circulating water channel. Furthermore, CFD analysis on the model of the present hydropower system was conducted to estimate the power

generation performance in a wide range of parameters.

As the first step, we fabricated and tested an experimental model of the proposed system to investigate its feasibility and power generating performance. From the experimental results, we obtained the following conclusions: The power generating system for the generators using dielectric elastomers with 8 *cm* diameter can be driven well by the Karman vortices in a water flow; we have to select the diameter of the cylinder and the size of the wing corresponding to the fluid velocity in order to obtain high efficiency of this system; the maximum energy efficiency is about 43% in the present system, when the water velocity is 0.4 *m/s*, the cylinder diameter is 48 *mm* and the distance between the cylinder and the wing is 170 *mm*; the maximum average electric power of approximately 16 *mW* is verified with a generation efficiency of about 36%, when the span and chord length of the wing are 120 *mm* and 30 *mm*, respectively, the diameter of the cylinder is 60 *mm*, the distance between the cylinder and the wing is 170 *mm*, and the velocity of the water flow is 0.5 *m/s*.

Secondly, we focused on the oscillation of the wing that is directly associated with the generation performance in the proposed system. The drive characteristics of the wing and the flow fields around the wing were measured in a small circulating water channel. The measuring results show that the wing vibration frequency agrees very well with the vortex shedding frequency, the wing oscillation amplitude becomes largest, i.e., the resonance amplitude, at a reduced velocity of approximately 5, and vortices which drive the wing are not fully developed near the cylinder owing to a dead water region.

Two-dimensional CFD analysis was carried out for the small hydropower generation system proposed in this study to evaluate its generation performance in a wide range of parameters. The wing oscillations behind a circular cylinder which generates Karman vortices were simulated and the results were compared with the experimental data. Although the computational results show that the frequency of wing oscillation tends to be approximately 15% larger than the experimental results, the simulation result of a flow pattern corresponds well to the experiment when the oscillation amplitude of the

CFD result is close to the resonance amplitude of the experiment. Therefore, by improving the accuracy of simulation (such as three-dimensional simulation), we can expect that the power generation performance of the system is predicted well by CFD.

We presented the characteristics of the power generating system for dielectric elastomers driven by Karman vortex street and estimated its electric power generation in this study. The proposed system consists of a simple structure and can be expected to be used at various locations in the future.

CONTENTS

LIST OF FIGURES

LIST OF TABLES

ACKNOWLEDGMENTS

First of all, the author would like to express his deepest and most sincere gratitude to his academic supervisor, Professor Takanori Hino, for his continuous guidance, cooperation, encouragement and sharing valuable time throughout this work. It is also much pleasure to acknowledge his untiring help by supplying supporting valuable references and information, without which this work could not have been completed.

The author expresses his gratefulness to Professor Y. Kawamura, Associate Professor Y. Nishi and Associate Professor Y. Hirakawa for their valuable suggestions, comments, and help with study materials throughout his study. Special thanks go to thesis committee member, Professor K. Suzuki, for his valuable comments and suggestions which certainly improve the quality of this work. Sincere thanks extend to the following person for his technical assistance, in particular to Mr. S. Michiyama who always provided excellent ideas and valuable time. The author also wishes to thank for their consistent help in a very friendly atmosphere from the all students of the Smart Structure and Systems laboratory and the Hydrodynamics laboratory.

The author greatly acknowledges the scholarship sponsored by Yokohama National University.

The author is deeply indebted to his parents, girlfriend and other relatives for their encouragements and supports. Finally, the author expresses his thanks to all the concerned persons who either directly or indirectly helped him in various ways to complete this thesis.

CHAPTER 1

INTRODUCTION

Today, there is a great expectation that power generation systems utilizing renewable energy sources will come into wide use owing to depletion of fossil fuel resources, environmental pollution and population increase [1)]. Renewable energy is derived from natural processes that are replenished constantly. The main sources of renewable energy are hydropower, solar, wind, biomass, geothermal, etc.

1.1 Hydropower Generation

1.1.1 Current State

Hydropower is a renewable energy source that has been utilized for electricity production since late 19th century [2)]. The kinetic energy of falling water is used to generate electricity in hydropower plants. Turbines capture the kinetic energy of water by rotating with water pressure. The rotation energy is converted into electric energy by power generators.

Hydropower provides over 16% of global electricity production [3)], and China, Canada, Brazil and the USA account for about 46% of the production of hydropower generation in the world [4)]. With policy support of governments for new hydropower construction, hydropower industry is expected to be more active [5)].

Hydropower plants are classified in three main categories according to the facility type, which are run-of river hydropower plants, storage hydropower plants, and pumped storage hydropower plants. In addition, hydropower plants can also be categorized

based on their capacities. Classification according to size has led to concepts such as small hydropower generation and large hydropower generation, based on installed capacity. Small-scale hydropower plants are expected to be run-of-river facilities than larger hydropower plants. Compared to large-scale hydropower, it typically takes less time and efforts to construct and integrate small hydropower schemes into local environments [6]. For this reason, the deployment of small-scale hydropower plants is increasing in many parts of the world, especially in remote areas where other energy sources are not viable or are not economically attractive.

1.1.2 Small-scale Hydropower Generation

Although large-scale hydropower generation is the mature technology, a number of studies have been performed to develop small-scale hydropower generation today [7)-11)]. Conventional electric generators using electromagnetic induction, however, may not be suitable to down-scaling. These electric generators tend to operate most efficiently in a narrow range of high frequencies. Accordingly, electricity generation systems by electric generators using electromagnetic induction include a mechanical or hydraulic transmission, resulting in more complex and larger systems.

1.2 Objective

We focused on dielectric elastomers (DEs) that are a new transducer technology to create a simple and efficient system for small-scale hydroelectricity, and proposed a power generating system for dielectric elastomers driven by Karman vortex street. This system extracts mechanical energy from fluid energy using the vibration of a wing which is set in the Karman vortex street in response to hydrodynamic force. The mechanical energy is transmitted to a DE generator through a shaft and subsequently converted into electrical energy. The objectives of this dissertation are as follows:

(1) To experimentally investigate the feasibility and the power generating

performance of the proposed power generating system.

(2) To show the characteristics of the present system by measuring the motion of the wing and the flow fields around the wing.

(3) To evaluate the generation performance of the proposed system in a wide range of parameters by CFD analysis.

1.3 Overview of the Dissertation

This dissertation is composed of six chapters. In Chapter 1 the general outline of the thesis and introductory notes are presented.

In Chapter 2 we propose a power generating system for dielectric elastomers driven by Karman vortex street. The basic information about dielectric elastomers and Karman vortex street are described, and the configuration of the proposed system is presented.

In Chapter 3 we fabricate and test an experimental model of the present system to investigate its feasibility and the power generating performance. The experimental results are shown and the scale-up of the system is discussed.

In Chapter 4 we focus on the oscillation of the wing that is directly associated with the generation performance in the proposed system. The drive characteristics of the wing and the flow fields around the wing are measured in a small circulating water channel.

In Chapter 5 we carry out two-dimensional CFD analysis for the small hydropower generation system proposed in this study. The wing oscillations behind a circular cylinder which generates Karman vortices are simulated and the results are compared with the experimental data obtained in Chapter 4.

In Chapter 6 we summarize the conclusions and future work.

CHAPTER 2

PROPOSAL FOR POWER GENERATING SYSTEM USING DIELECTRIC ELASTOMERS DRIVEN BY KARMAN VORTEX STREET

We focus on dielectric elastomers that are a new transducer technology to innovate small-scale hydroelectric power generating system and propose the new simple system using a dielectric elastomer, which is driven by Karman vortex street. This system extracts mechanical energy from fluid energy by vibration of a wing which is set in the Kaman vortex street in response to hydrodynamic force. The mechanical energy is transmitted to a dielectric generator through a shaft and subsequently converted into electrical energy.

2.1 Dielectric Elastomer

2.1.1 Background

Dielectric elastomer (DE) is a new transducer technology that has been under development by many researchers since Pelrine and Chiba [12] proposed DE in 1991. The element of DE is a very simple structure comprised of a thin elastomer sandwiched by two compliant electrodes [13)-15)]. DE is often used as an actuator. The both electrodes of DE are attracted to each other by Coulomb forces when a voltage difference is applied between them, resulting in a thickness-wise contraction and plane-wise expansion of the elastomer. Recently, the use of DE actuators in the reverse mode, in which deformation of the elastomer by external force is used to generate electric energy, has attracted attention as a new method for taking out electric energy from renewable energy [16)-19)].

2.1.2 Dielectric Elastomer Generator Fundamentals

DE generates electricity in reverse operation of its actuation mode, in which DE can be considered to be a variable capacitor having constant volume [16].

Figure 2.1 shows the operation principle of DE generator. When mechanical energy is applied to DE, DE is stretched, which means compression in thickness and expansion of the surface area, and electric charge is stored on the membrane (Figure 2.1a). When the mechanical energy is subsequently unloaded, the elastic recovery force of the DE acts to restore the original thickness and area (Figure 2.1b). At this moment, the electric charge is pushed out the electrode direction. This change of the electric charge increases the voltage difference, resulting in an increase of electrostatic energy.

(a)

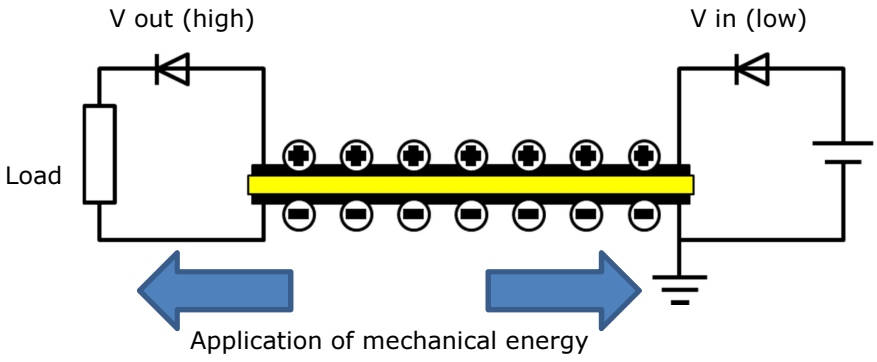

(b)

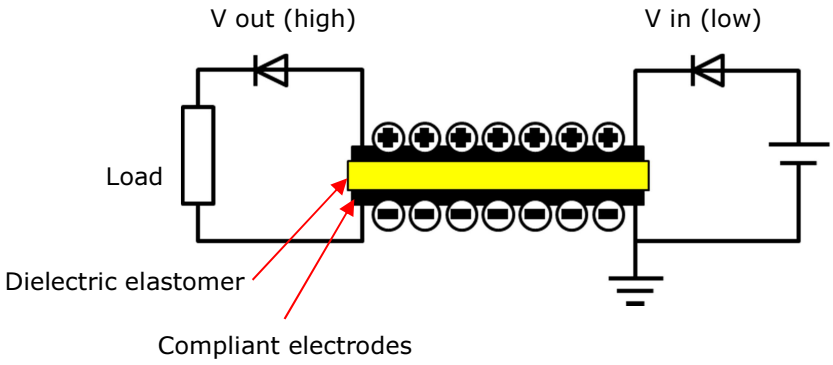

Figure 2.1 Operation principle of DE generator [19]. (a) DE is stretched by application of mechanical energy, (b) DE is relaxed.

The capacitance (C) of a DE film is written as the following equation [16)-18)]:

$$C = \varepsilon_0 \varepsilon \frac{A}{t} = \varepsilon_0 \varepsilon \frac{b}{t^2} \tag{2.1}$$

where ε_0 is the dielectric permittivity of free space, ε is the dielectric constant of the DE film, A is the active polymer area, t is the thickness of the DE and b is the volume of the DE. The second equality in Equation 2.1 can be written because the volume of the DE is essentially constant.

With respect to the changes of voltages, the electric charge (Q) on a DE film is considered to be constant in the basic circuit and over a short period of time. Since $V = Q/C$ where V is the voltage, the relation between the voltage in the stretched state (V_2) and the contracted state (V_1) can be expressed as:

$$V_2 = \frac{Q}{C_2} = \frac{C_1}{C_2}\frac{Q}{C_1} = \frac{C_1}{C_2} V_1 \tag{2.2}$$

where C_1 and C_2 are the total capacitances of the DE films in the stretched state and contracted state, respectively. V_2 is higher than V_1 because of $C_2 < C_1$. V_2 obtained by Equation 2.2 is in excellent agreement with experimental data based on high impedance measurements [19)].

The energy output (E) of a DE generator per cycle of stretching and contraction is associated with the difference in the capacitance between the stretched and contracted states as the following equation:

$$E = \frac{1}{2} C_1 V_b^2 \left(\frac{C_1}{C_2} - 1 \right) \tag{2.3}$$

where V_b is the bias voltage. The amount of energy generated by a DE generator is determined by its maximum strain and its dielectric breakdown strength. Energy densities of DE generators using polymer materials such as acrylic and silicone elastomers have been produced more than an order of magnitude greater than energy densities of electromagnetic or piezoelectric materials [17]. In addition to high energy density, these equations exhibit that the efficiency of the energy conversion is not directly related to the frequency of operation. Generators using DE are related to its deformation volume and do not require rapid deformation as in the case of a piezoelectric element. Therefore, DE generators can be expected to generate electricity efficiently in the range of low frequency motion such as human activity or ocean waves.

2.1.3 Wave Power Generation using Dielectric Elastomer Generator

SRI International and HYPER DRIVE Corp. [18] mounted the generator using a DE of 300 *g* on a buoy for weather observation and carried out the world's first marine experiment on power generation by actual sea waves for two weeks in 2007 in the Tampa Bay, USA. Figure 2.2 shows the buoy mounted with the DE generator used in the experiment. The generating unit was a cylindrical shape with 40 *cm* in diameter and 1.2 *m* in height, in which two roll-type DE modules having a diameter of 30 *cm* and a height of 20 *cm* in the stretched state were installed. Although the maximum energy output of 40 *J* per stroke was measured in laboratory tests, the peak and average power of 11 *W* and 1.2 *W*, respectively, were produced due to low waves of about 10 *cm* in the Tampa Bay.

Chiba et al. [19] tested a simple scale model of DE-based wave energy harvesting system in a wave tank over a range of wave periods from 0.7 to 3.0 *s* and wave heights from 2 to 6 *cm* in order to explicitly demonstrate that the amount of energy generated by a DE generator is independent of the frequency of operation. The employed generating unit consisted of a linear motion diaphragm-type DE transducer that incorporated 2.8 *g* of active polymer material. The active polymer was made from the acrylic polymer (3M

Corp. VHB4910) and the electrode was made of carbon black. Eight active polymers with an annular rig shape with a 100 *mm* outer diameter were used for the DE-based electric generator. This DE generator had a maximum energy generation capability of approximately 46.58 *mJ* per stroke. The reaction force necessary for the maximum energy generation output was 47.53 *N*. Consequently, they show that the energy output is largely independent of wave period and the maximum electricity generated in one wave is 42 *mJ* for the wave height of 6 *cm*.

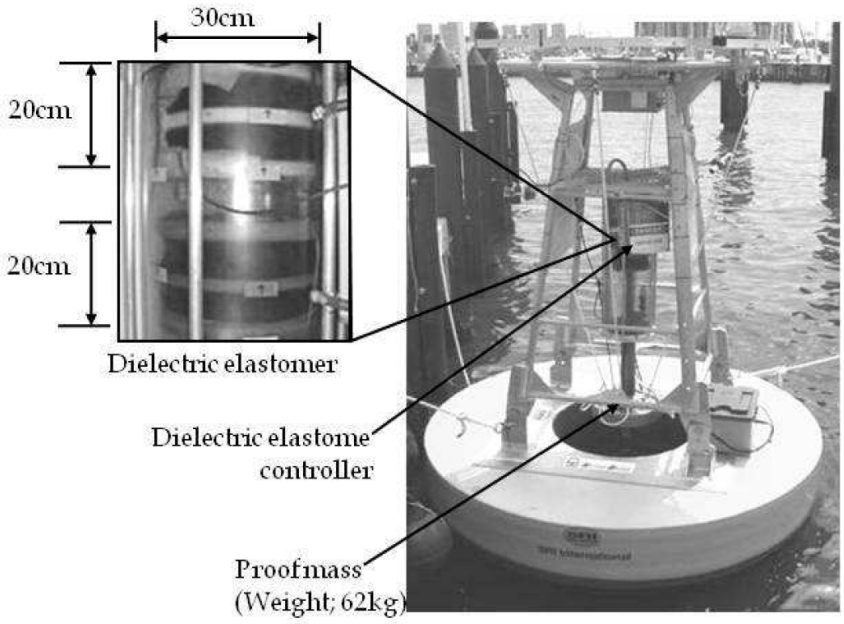

Figure 2.2 Weather observation buoy mounted DE generator for wave power generation [20].

2.2 Karman Vortex Street and Its Use for Power Generation

2.2.1 Basic phenomenon

Karman vortex street is a series of vortices shed periodically in the wake of a bluff body as shown in Figure 2.3. The vortices are alternately formed on each side of the body and have opposite directions. These vortices do not mix with the outer flow and are dissipated by viscosity only after a long time. The Karman vortex street behind a cylinder occurs at Reynolds numbers (*Re*) from about 40 to 3.7×10^5 [21]. *Re* is a dimensionless value that measures the ratio of inertial forces to viscous forces and may be defined as:

$$Re = \frac{UD}{\nu} \tag{2.4}$$

where *U* is the steady velocity of the flow upstream of the cylinder, *D* is the diameter of the cylinder, and *v* is the kinematic viscosity of the fluid. The frequency at which vortices are shed behind a cylinder in a Karman vortex street is related to the Strouhal number (*St*) by the following equation:

$$St = \frac{f_v D}{U} \tag{2.5}$$

where f_v is the vortex shedding frequency. *St* is experimentally found to be approximately equal to 0.21 in $500 < Re < 3.7\times10^5$ for circular cylinders [21].

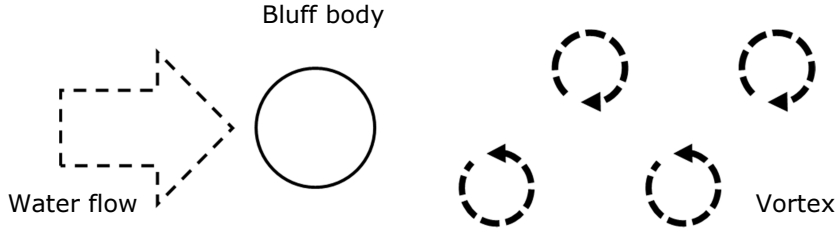

Figure 2.3 Karman vortex street.

2.2.2 Literature Review on Energy Harvesting from Karman Vortex Street

Allen and Smits [22] examined the feasibility of placing a piezoelectric membrane in the wake of a bluff body and using Karman vortex street forming behind the bluff body to induce oscillations in the membrane (Figure 2.4). The vibration results in a capacitive buildup in the membrane that provides a voltage source that is capable of trickle-charging a battery in a remote location.

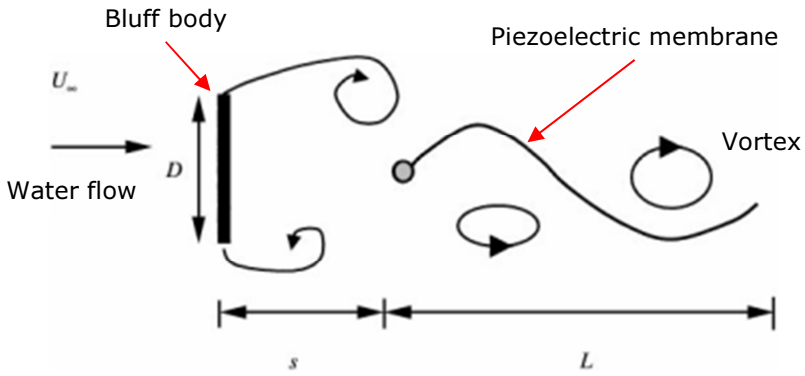

Figure 2.4 Schematic diagrams of energy harvesting device from Karman vortex street by Allen and Smits [22].

Zhu et al. [23] reported a novel cantilever-based electromagnetic wind generator for wireless sensing applications (Figure 2.5). The generator consists of a bluff body, a magnet, a coil, and an airfoil attached to a cantilever spring. The airflow over the airfoil causes the oscillating motion of the cantilever, resulting in the degree of bending being a function of the lift force from the airfoil and the spring constant. The permanent magnet is fixed on the airfoil and the coil is attached to the device. The motion of the airfoil causes the magnetic flux cutting the coil to change, which generates electrical power. The device has dimensions of 12 *cm* × 8 *cm* × 6.5 *cm*. Experimental results show that the device can operate at wind speeds as low as 2.5 *m/s* with a corresponding electrical output power of 470 μW, which means sufficient for periodic sensing and wireless transmission. When the wind speed is 5 *m/s* , the output power is 1.6 *mW*.

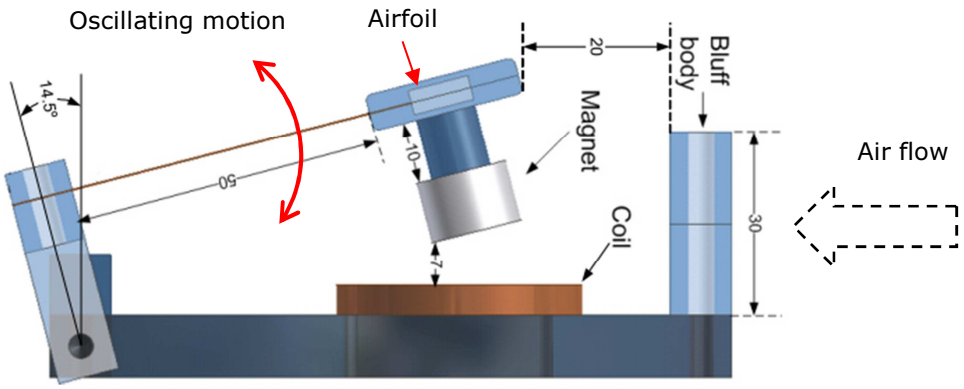

Figure 2.5 Schematic diagrams of energy harvesting device from Karman vortex street by Zhu et al. [23].

Akaydin et al. [24] evaluated the power generating performance of piezoelectric beams placed in the wake of a circular cylinder at high Reynolds numbers of 10,000 to 21,000 (Figure 2.6). The beam has dimensions of 30 *mm* × 16 *mm* × 0.2 *mm*, and the cylinder has a diameter of 0.03 *m* and a length of 1.22 *m*. The experiments were carried out in a wind tunnel. The maximum output power of about 4 μW was obtained at Re = 14,800 in the device.

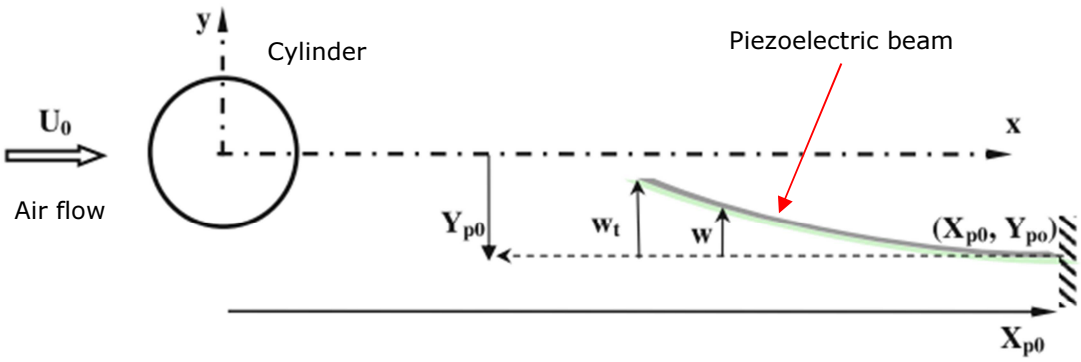

Figure 2.6 Schematic diagrams of energy harvesting device from Karman vortex street by Akaydin et al. [24].

Wang et al. [25] proposed a new electromagnetic energy harvester for harnessing energy from vibration induced by Karman vortex street (Figure 2.7). The variation of the liquid pressure in the wake of a bluff body drives a flexible diaphragm with an attached permanent magnet into vibration. The vibration energy is converted to electrical energy by electromagnetic induction. They fabricated and tested a prototype of the energy harvester having a volume of 37.9 cm^3. Experimental results show that the instantaneous power of 1.77 μW is generated under a pressure fluctuation frequency of 62 *Hz* and a pressure amplitude of 0.3 *kPa* in the Karman vortex street.

Wang et al. [26] also developed a new miniature hydro-energy generator using a cantilevered piezoelectric beam for harnessing energy from Karman vortex street behind a bluff body in a water flow. This system has almost the same as the structure shown in Figure 2.7 and can be capable of producing an output power of 0.7 *nW* when the pressure oscillates with an amplitude of nearly 0.3 *kPa* and a frequency of about 52 *Hz*.

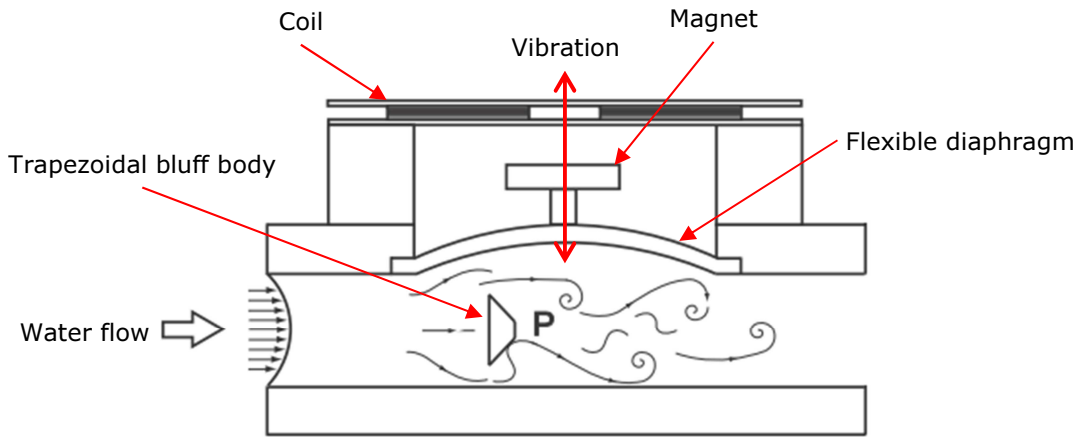

Figure 2.7 Schematic diagrams of energy harvesting device from Karman vortex street by Wang et al. [25].

Nguyen et al. [27] presented a miniature pneumatic energy generator for harnessing energy from Karman vortex street behind the bluff bodies in tandem arrangement to enhance the amplitude of the pressure fluctuation in the vortex street, which vibrates a piezoelectric film (Figure 2.8). Experimental results show that an average output power is 0.59 *nW* with a pressure oscillation amplitude of about 70 *Pa* and a frequency of nearly 872 *Hz*.

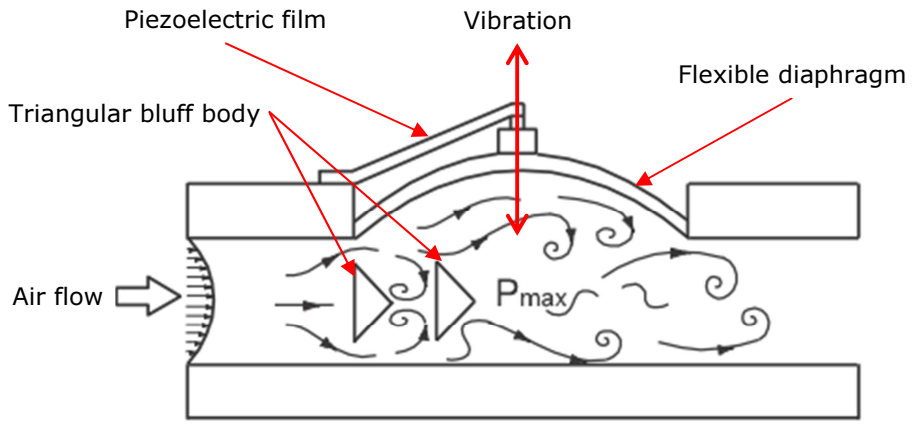

Figure 2.8 Schematic diagrams of energy harvesting device from Karman vortex street by Nguyen et al. [27].

Demori et al. [28] proposed an innovative energy harvesting system based on a piezoelectric converter to extract energy from airflow for autonomous sensors (Figure 2.9). The vibration of the blade induced by Karman vortex street results in generating power by the converter. Experimental results show that a harvested power of about 100 μW with retransmission intervals below 2 *min* is obtained.

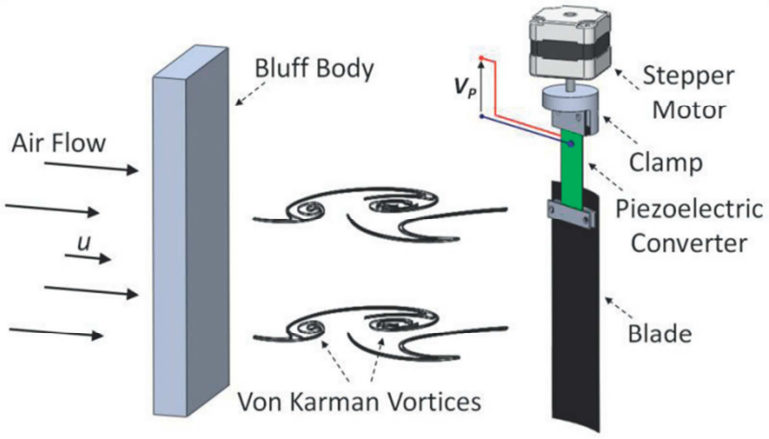

Figure 2.9 Schematic diagrams of energy harvesting device from Karman vortex street by Demori et al. [28].

2.3 Configuration of Proposed Power Generating System

On the basis of DE generators and Kaman vortex street, the small hydroelectric generation system was designed to create a simple system which is capable of generating electric energy efficiently also at low frequencies. Figure 2.10 shows a schematic diagram of the proposed system. The system mainly consists of two DE generators, a wing, a cylinder, a shaft and a fulcrum. The cylinder is fixed in a uniform water flow and generates Karman vortices. The wing and the DE generators are connected by the shaft through the fulcrum. Therefore, the motion of the wing results in operation of the generators.

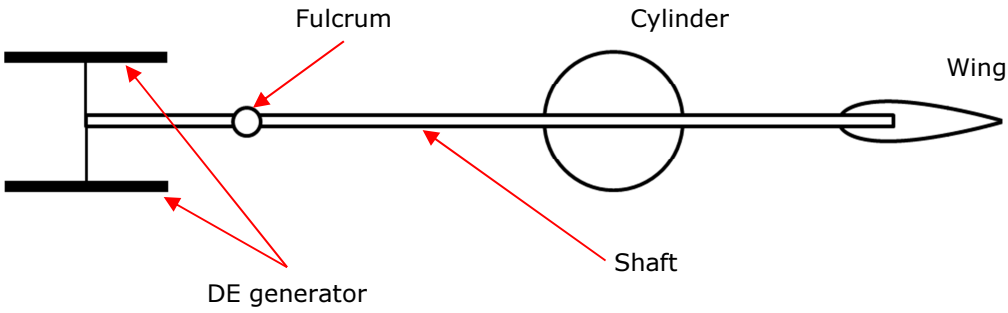

Figure 2.10 Schematic diagram of the small hydroelectric generation system proposed in this study.

2.3.1 Components

A generating unit supposed in this study is a diaphragm type DE generator with an 80 *mm* diameter. Figure 2.11a and Figure 2.11b show a photo and a cross section view of the DE generator, respectively. The black part in the photo is the DE film with a diameter of 80 *mm*. The center of the device is pushed and released to function. This generator produces electric energy of 8 *mJ* per stroke for the stroke length of 10 *mm* (Figure 2.11c).

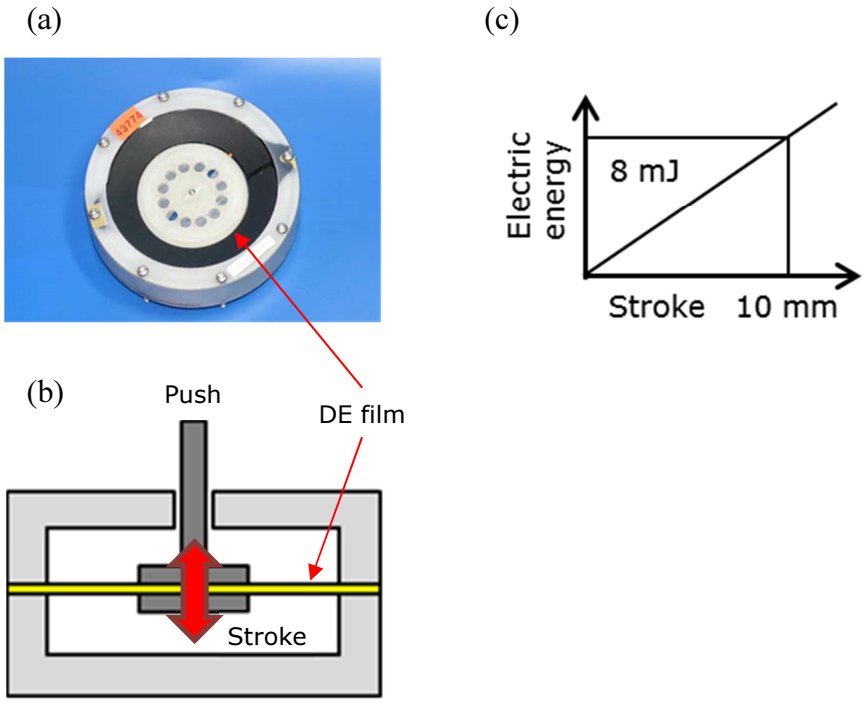

Figure 2.11 DE generator with a diameter of 80 *mm*. (a) Photo, (b) Cross section view, and (c) Generated electric energy as a function of stroke.

In order to extract mechanical energy from fluid energy, a wing is set downstream of a cylinder and made to oscillate due to pressure fluctuation of the vortex street. The wing has a cross-sectional shape of NACA0021 as shown in Figure 2.12 to provide the DE generators with a stroke amplitude efficiently. It is important to obtain large amplitude

oscillation since DE generators produce electric energy proportional to the stroke amplitude and therefore the wing shape is selected for its superior lift characteristics.

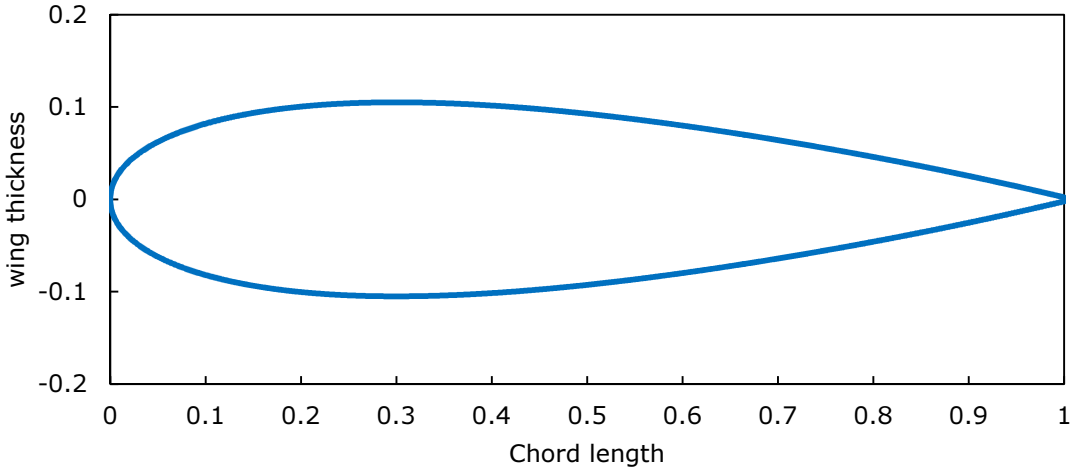

Figure 2.12 Cross-sectional view of wing with NACA0021.

2.3.2 Operational Principle

The operation principle of the generating system proposed in this study is illustrated in Figure 2.13. The cylinder fixed in a water flow generates Karman vortices (Figure 2.13a). The wing vibrates, driven by the pressure in the vortex, resulting in a stroke of the DE generator (Figure 2.13b). In this system, the wing moves with one degree of freedom, i.e., the rotation around the rotation axis. Therefore, the equation of motion is expressed as:

$$I\ddot{\theta} + C\dot{\theta} + K\theta = M_z \tag{2.6}$$

where θ is the rotation angle (Figure 2.13c), I is the moment of inertia, C is the damping coefficient, K is the torsion spring coefficient, and M_z is the hydrodynamic moment.

Since this wing motion consists of interaction among the DE generator, the wake flow of a cylinder and vortices generated by the wing vibration, Equation 2.6 is difficult to solve theoretically. Therefore, performance and characteristics are found out by experiments and CFD simulations in this study.

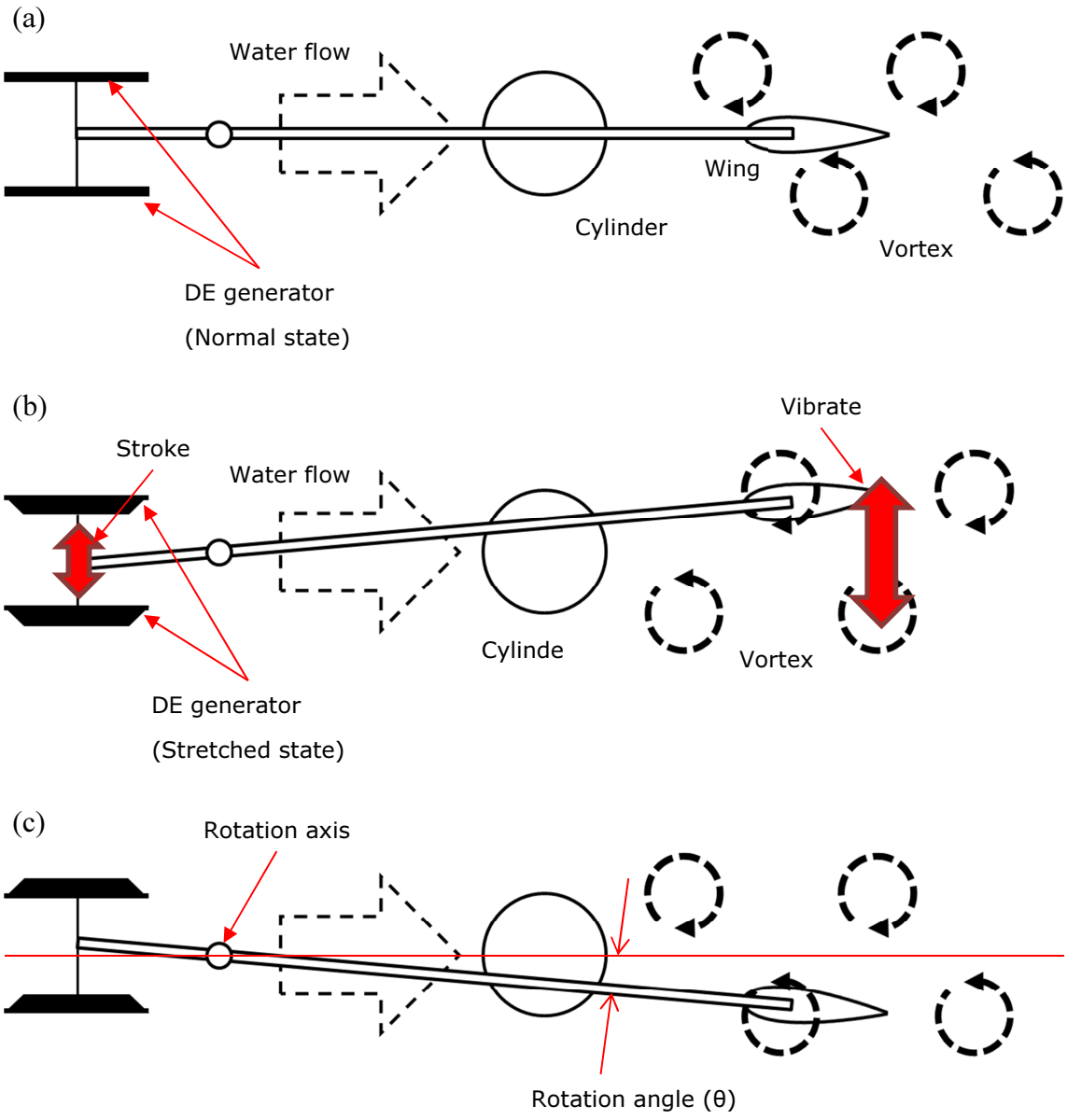

Figure 2.13 Operation principle of the proposed generating system.

CHAPTER 3

PRESUMPTION OF POWER GENERATION PERFORMANCE BY EXPERIMENT

In order to verify the feasibility and estimate the power generation performance of the proposed hydroelectric power generation system using the DE generators as shown in Figure 2.11 experimentally, the model is fabricated and tested.

3.1 Experiment

3.1.1 Setup

The two-dimensional small circulating water channel used in this study is shown in Figure 3.1. It has an acrylic observation part with 1,000 *mm* in length, 300 *mm* in width and 200 *mm* in water depth. Water velocity (U) was set at 0.30 to 0.70 *m/s* by 0.05 *m/s*, which corresponds to approximately $1.8\times10^4 < Re < 5.3\times10^4$ where the Reynolds number (Re) is defined in Equation 2.4. A cover of the circulating water channel is capable of reducing the free surface effect and installing experimental equipment.

Figure 3.2 shows a schematic drawing of the experimental apparatus, which are fixed on the cover of the circulating water channel. A cylinder made of vinyl chloride are employed as bluff bodies to generate a Karman vortex street. The height of the cylinder is 290 *mm* and the diameters (D) are 48, 60 and 76 *mm*. In this experiment, a DE spring, which has the same spring constant with DE generators with a diameter of 80 *mm* (Figure 2.11), is used in place of the DE generator. The two DE springs are fixed 470 *mm* ahead of the cylinder. The shaft made of aluminum is put between the DE springs through the fulcrum located 370 *mm* ahead of the cylinder. Therefore, the DE springs

are deformed due to the movement of a wing, which is set in the region where the Karman vortices are formed. It is noted that the shaft is suspended from above with a string having 400 *mm* in length so as to prevent the shaft from leaning. The wing has a cross-sectional shape of NACA0021 (Figure 2.12), a span (*s*) of 120 *mm* and a chord length (*c*) of 30 *mm*, which is made from epoxy resin. This wing converts fluid energy into mechanical energy by oscillating because of Karman vortices. Figure 3.3 shows a photo of the fabricated experimental model which is set in the circulating water channel.

Figure 3.1 Photo of the circulating water channel used in this study.

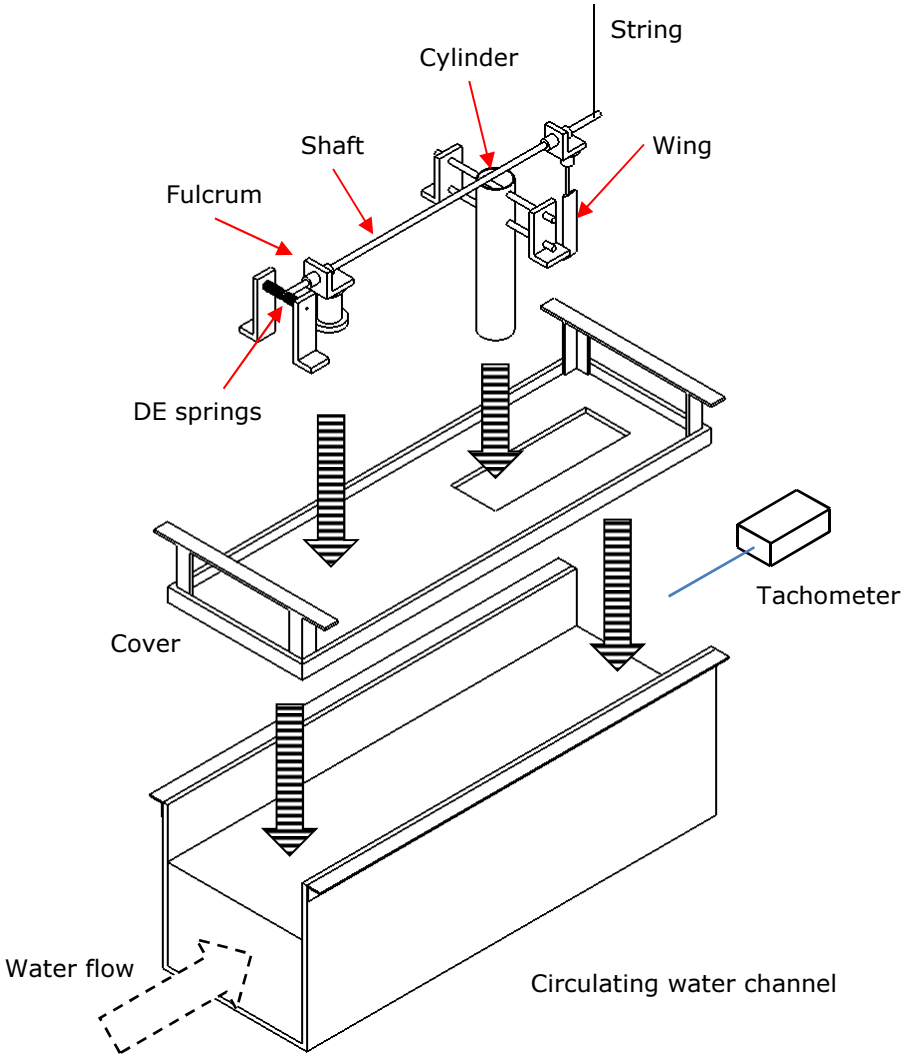

Figure 3.2 Schematic drawing of the fabricated system.

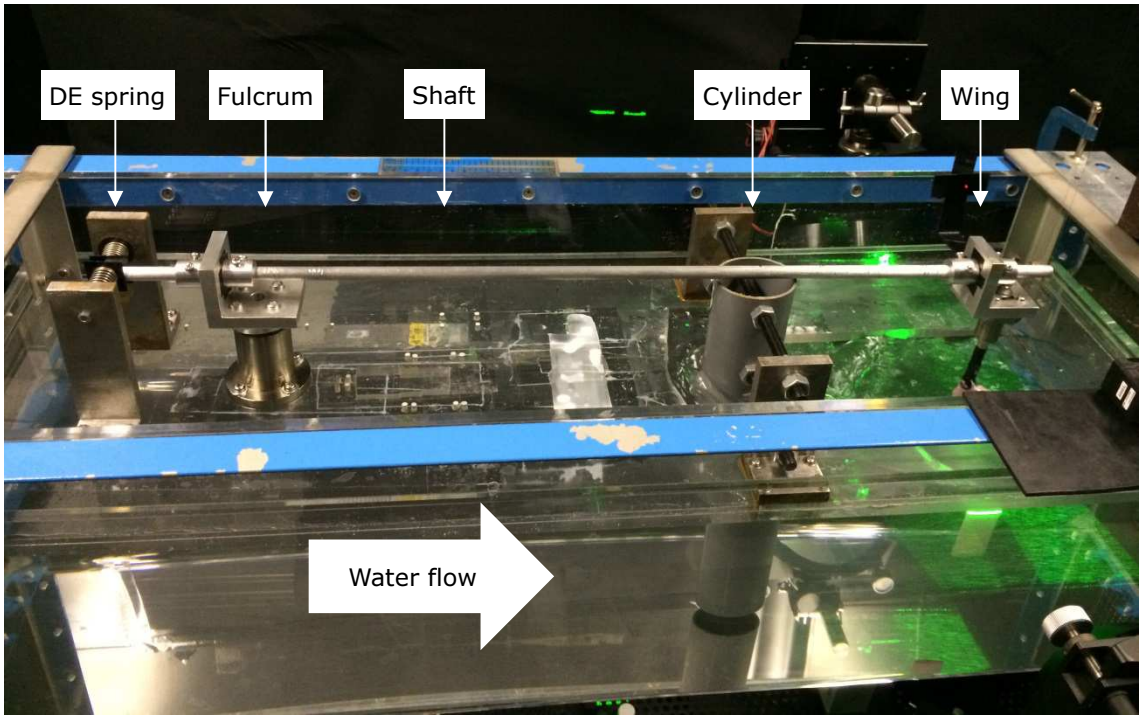

Figure 3.3 Photo of the fabricated experimental model.

3.1.2 Measuring Instrument and Estimation Method

In order to estimate the power generation performance of the proposed system, the stroke amplitude of the DE springs and the oscillation frequency are measured.

A reflective tape is attached at the fixture for fixing the wing to the shaft so as to gauge a wing oscillation frequency in each amplitude range with a laser beam digital tachometer (DT-6234B, Vellman nv) installed behind of the wing. The vibration frequency at the wing oscillation amplitude (a) corresponding to each stroke of the DE springs (z = 1, 2, 3...12) was measured by adjusting an irradiation point of the laser beam as shown in Figure 3.4. a can be determined according to the installed place of the wing. The number of the wing reciprocation was measured for 3 minutes and divided by the measurement time to obtain the DE spring frequency (f) coincides with the wing frequency.

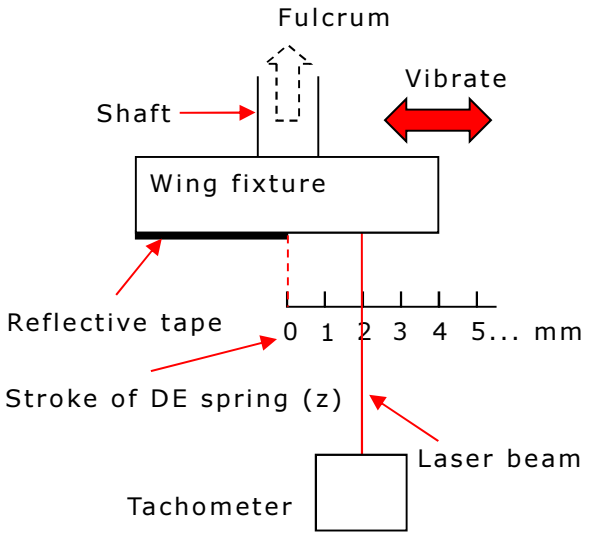

Figure 3.4 Schematic view of the measuring system (top view).

The estimated power generation of this system is calculated by using the frequency (f) and the stroke amplitude (z) of the DE springs. The DE generator assumed in this study have the power generation performance shown in Figure 2.11c. Therefore, the electric power generation (P) of our system is expressed as the following equation:

$$P = nWzf \tag{3.1}$$

where n is the number of generating unit (2 units), W is the power generation performance (0.8 *mJ/mm*) of the DE generator (Figure 2.11c). However, $P = 0$ *W* for z is smaller than 4 *mm* owing to the character of the DE generator.

The input energy (E_{in}) to this system is assumed to be:

$$E_{in} = \frac{1}{2}\rho A U^3 \tag{3.2}$$

where ρ is water density and A is the project area of the wing (765 mm^2). The energy conversion efficiency (η), i.e., the total efficiency, of this system is expressed as:

$$\eta = \frac{P}{E_{in}} = \frac{nWzf}{1/2\,\rho A U^3} \tag{3.3}$$

3.2 Test conditions

To examine where the effective position of the wing for producing electricity locates, the distance between the cylinder and the wing (l_{cw}) was varied from 50 to 210 *mm* by 10 *mm* for each water velocity (U = 0.3 to 0.7 *m/s*). Furthermore, tests were conducted for the case of three cylinders with diameters of 48, 60 and 76 *mm* to confirm the size relationship between the cylinder and the wing.

3.3 Results and Discussion

3.3.1 Oscillation Frequency and Stroke

Figure 3.5 shows the frequency of Karman vortex generation (f_v) and the vibration of the DE springs (f) for a cylinder diameter (D) of 60 *mm* and the distance between the cylinder and the wing (l_{cw}) of 170 *mm*. It is noted that the theoretical f_v from Equation 2.5 corresponds well to the experimental results of f when U is less than 0.6 *m/s*, which means that the driving force of the DE springs came from the pressure of vortex. Also, when U is larger than 0.65 *m/s*, measuring accuracy becomes inferior because the wing oscillation amplitude becomes smaller.

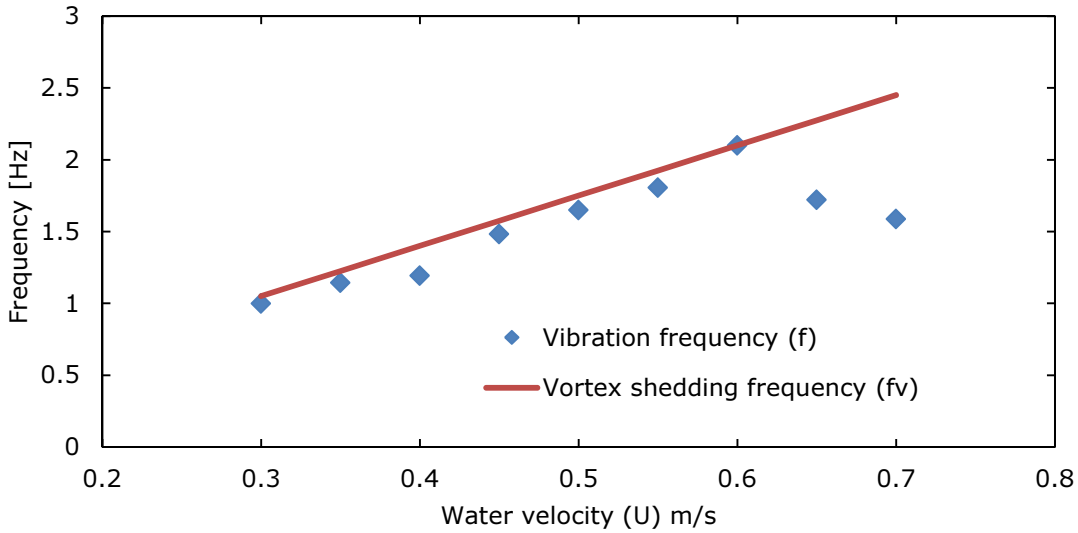

Figure 3.5 The frequency of Karman vortex generation (f_v) and the vibration of the DE springs (f) for a cylinder diameter (D) of 60 *mm* and the distance between the cylinder and the wing (l_{cw}) of 170 *mm*.

Figure 3.6 shows the histogram of vibrational components of the DE springs in this system for a cylinder diameter (D) of 60 *mm* and the distance between the cylinder and the wing (l_{cw}) of 170 *mm*, and water velocities (U) of 0.4, 0.5 and 0.6 *m/s*. The stroke amplitude of the DE springs (z) is found not to be constant per unit stroke of the DE springs. For a water velocity (U) of 0.4 *m/s*, the wing and the DE springs oscillated at a frequency of about 1.2 *Hz* (Figure 3.5). In this vibration of the DE springs, z of 4 *mm* per unit stroke accounts for approximately 60% of the vibration, and z of 5 *mm*, 3 *mm* account for about 25% and 15%, respectively. For U = 0.5 *m/s*, f is approximately 1.7 *Hz* (Figure 3.5). z of 6 *mm* and 7 *mm* per unit stroke account for about 80% of the vibration, and z of 5 *mm* accounts for the rest. When U becomes 0.6 *m/s*, the DE springs oscillate with f of about 2.1 *Hz* (Figure 3.5). The vibrational components of the DE springs are dispersed from z of 1 *mm* to 5 *mm* with about 20%. The unstable wing oscillation for U = 0.6 *m/s* is assumed to be caused by strong turbulence in the wake of the cylinder. Therefore, z for U = 0.6 *m/s* becomes smaller than that for U = 0.5 *m/s*.

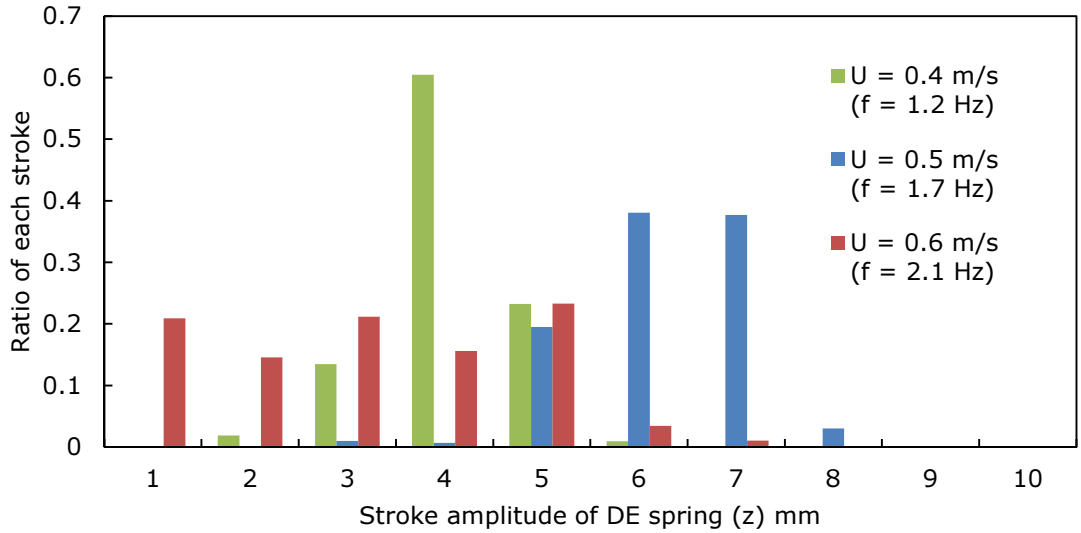

Figure 3.6 Histogram of vibrational components of the DE springs for a cylinder diameter (D) of 60 *mm*, the distance between the cylinder and the wing (l_{cw}) of 170 *mm*, and water velocities (U) of 0.4, 0.5 and 0.6 *m/s*.

3.3.2 Electric Power and Generating Efficiency

Figures 3.7-3.9 show the electric power generation (P) obtained by the experimental results and Equation 3.1 for cylinder diameters (D) of 48, 60 and 76 *mm*. For D = 48 *mm* shown in Figure 3.7, P becomes maximum and its value is about 11.6 *mW*, when the distance between the cylinder and the wing (l_{cw}) is 170 *mm* and the water velocity (U) is 0.45 *m/s*. For D = 60 *mm* shown in Figure 3.8, P becomes maximum and its value is about 16.3 *mW*, when l_{cw} is 170 *mm* and U is 0.5 *m/s*. For D = 76 *mm* shown in Figure 3.9, P becomes maximum and its value is about 12.7 *mW*, when l_{cw} is 190 *mm* and U is 0.5 *m/s*.

We can say that only one peak exists in each diagram about the electric power generation as shown in Figures 3.7-3.9. Therefore, in this system, we have to choose the condition of this peak, i.e., the combination of U and l_{cw}, to get the largest electric generation. Also we have to apprehend that there is almost no electric generation if the conditions are far from the peak in the diagram in this system. It is considered that the

maximum of P corresponds to kinds of the self-induced vibration or the resonance resulting from the combined effect of the water fluid dynamics and elastic deformation of the DE springs. In addition, vortices which drive the wing are not fully developed near the cylinder and become weak due to fluid viscosity far from the cylinder. It is noted that computational analysis would be effective to find the best condition about U and l_{cw} to get highest value of the electric generation and this is carried out in Chapter 5.

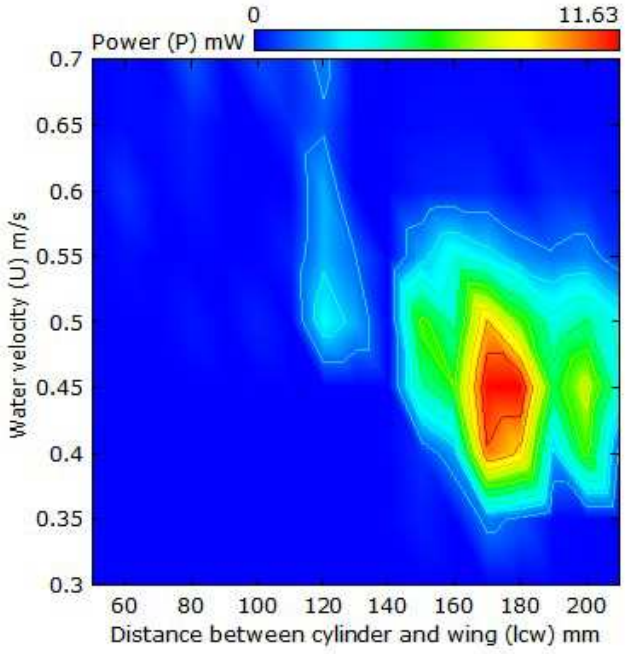

Figure 3.7 The electric power generation (P) for a cylinder diameter (D) of 48 *mm*.

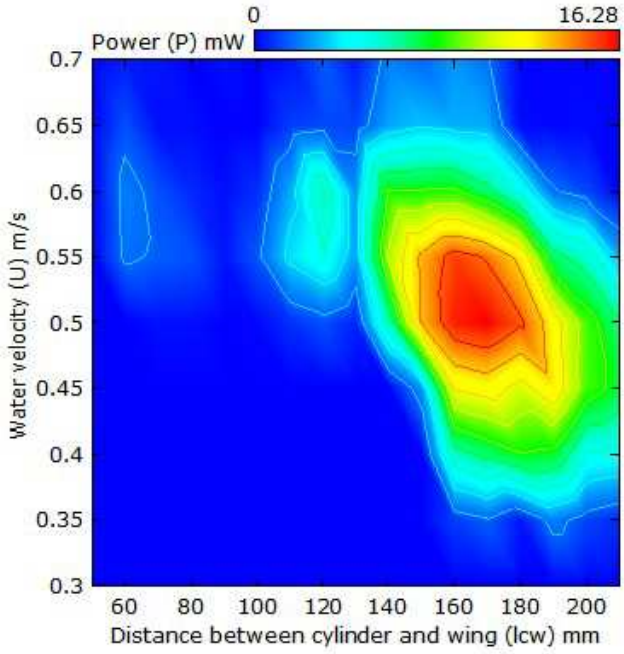

Figure 3.8 The electric power generation (P) for a cylinder diameter (D) of 60 *mm*.

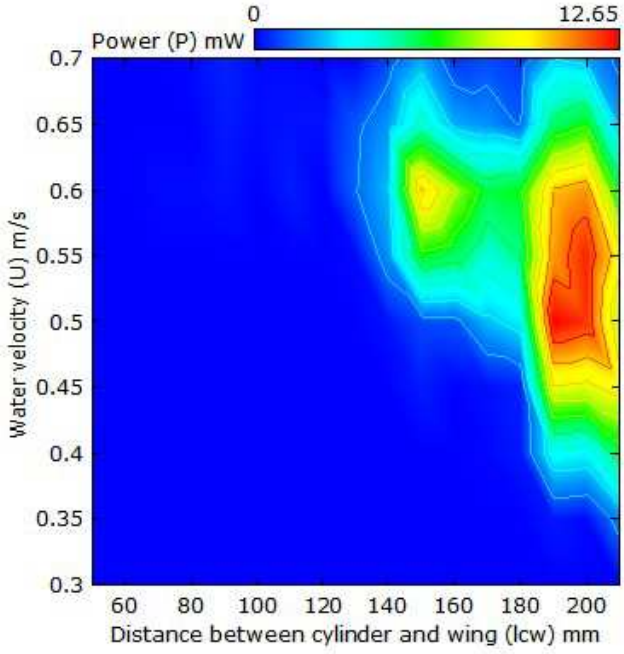

Figure 3.9 The electric power generation (P) for a cylinder diameter (D) of 76 *mm*.

Figures 3.10-3.12 show the results of the energy conversion efficiency (η) obtained by Equation 3.3 for cylinder diameters (D) of 48, 60 and 76 *mm*. For D = 48 *mm* shown in Figure 3.10, the energy conversion efficiency (η) becomes maximum and its value is about 43%, when the distance between the cylinder and the wing (l_{cw}) is 170 *mm* and the water velocity (U) is 0.4 *m/s*. For D = 60 *mm* shown in Figure 3.11, η becomes maximum and its value is about 36%, when l_{cw} is 180 *mm* and U is 0.5 *m/s*. For D = 76 *mm* shown in Figure 3.12, η becomes maximum and its value is about 27%, when l_{cw} is 190 mm and U is 0.5 *m/s*. It is noted that the maximum peak points of the diagram, i.e., the values of l_{cw} and U, in Figures 3.7-3.9 roughly correspond to those for Figures 3.10-3.12.

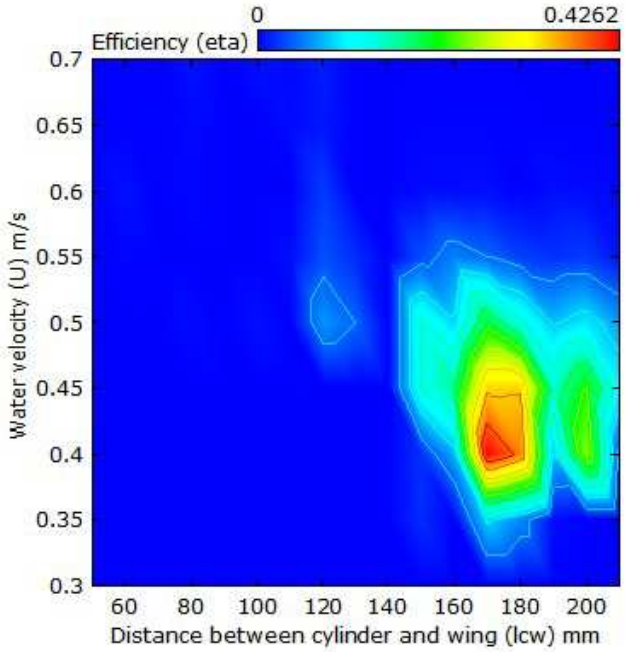

Figure 3.10 The energy conversion ratio (η) for a cylinder diameter (D) of 48 *mm*.

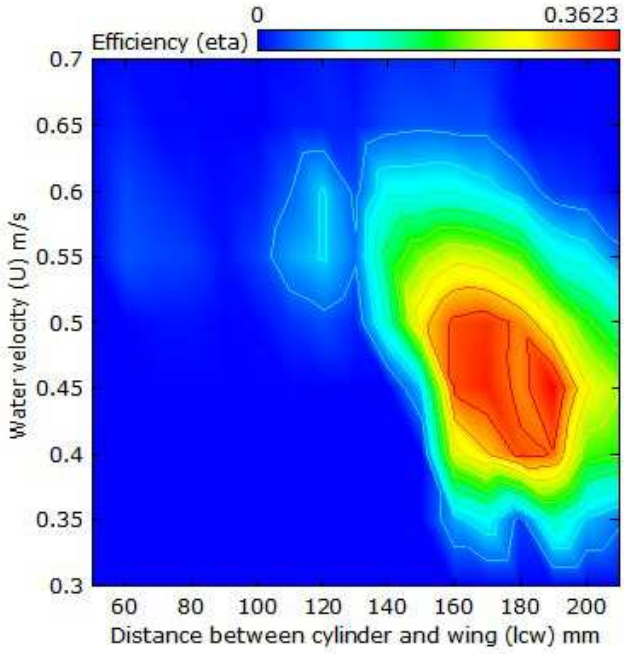

Figure 3.11 The energy conversion ratio (η) for a cylinder diameter (D) of 60 *mm*.

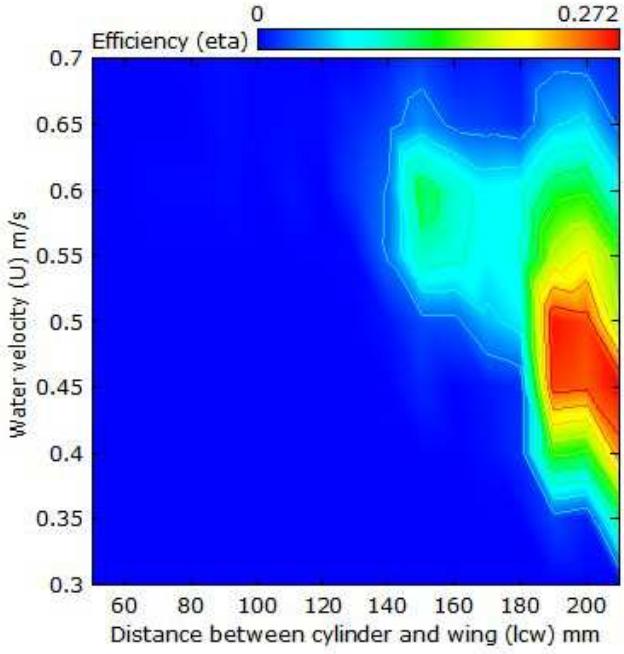

Figure 3.12 The energy conversion ratio (η) for a cylinder diameter (D) of 76 *mm*.

3.3.3 Scale-up of the System

Experimental results show such a low power generation as the proposed system can supply power to small remote sensing devices. Now, we estimate electric power produced by scaling up the system so that larger power generation for something such as street lamps is obtained.

The experimental conditions in which the maximum power generation (P) of 16.3 *mW* is obtained are as follows: a cylinder diameter (D) of 60 *mm*; the distance between the cylinder and the wing (l_{cw}) of 170 *mm*; a water velocity (U) of 0.5 *m/s*. The wing used in this study has a cross-sectional shape of NACA0021, a chord length (c) of 30 *mm* and a span length (s) of 120 *mm*. Under these conditions, the wing and the DE springs oscillate at a frequency of about 1.7 *Hz* (Figure 3.5). Since the driving force (T), which gives a stroke to the DE generators (the DE springs in this study), is obtained by the characteristics of the DE generator (Figure 2.11) and corresponds to the lift (L) acting on the wing in terms of the moment around the fulcrum, L is expressed as:

$$L = \frac{l_{sf}}{l_{cw} + l_{fc}} T \tag{3.4}$$

where l_{sf} is the distance between the DE springs and the fulcrum (100 *mm*) and l_{fc} is the distance between the fulcrum and the cylinder (370 *mm*). Moreover, L is non-dimensionalized by the dynamic pressure ($1/2\rho U^2$) and the wing area (cs) as the following equation:

$$C_L = \frac{L}{1/2 \rho U^2 cs} \tag{3.5}$$

where C_L is the lift coefficient and ρ is the fluid density. The non-dimensionalized values of this system in which the electric power generation becomes maximum are shown in Table 3.1.

Table 3.1 Non-dimensional parameters of the device for the maximum electric power of about 16.3 *mW*.

D/c	l_{cw}/c	l_{sf}/c	l_{fc}/c	s/c	Re	St	C_L
2	5.67	3.33	12.33	4	1.5×10^4	0.21	2.82

Power generation (P) is estimated by varying the chord length (c) of the wing under the conditions shown in Table 3.1. First, systems must be geometrically similar, that is, a cylinder diameter of $D = 2c$, the distance between the cylinder and the wing of $l_{cw} = 5.67c$, the distance between the DE generators and the fulcrum of $l_{sf} = 3.33c$, the distance between the fulcrum and the cylinder of $l_{fc} = 12.33c$, a wing span length of $s = 4c$. Second, since similarity of Reynolds and Strouhal number cannot be simultaneously satisfied, we focused on Strouhal number (St) for kinematic similarity because periodic vibration induced by vortices is considered as the most important parameter in this system. As the synchronization between a vortex shedding frequency (f_v) and a natural frequency (f_n) is very important to obtain high power generation, the water velocity (U) is set to be $U = f_nD/St = 2cf_n/0.2$ from Equation 2.5. Consequently, the wing vibrates at a frequency of $f = f_v = f_n$ in accordance with Karman vortices periodically generated at a frequency of $f_v = f_n$. It is noted that St is approximately 0.2 in $500 < Re < 3.7\times10^5$ in circular cylinders, which means that the wing chord length (c) must satisfy $25v < c^2f_n < 1.85\times10^4v$ from Equation 2.4. Finally, using Equations 3.4 and 3.5, the driving force (T) can be obtained.

Figures 3.13 and 3.14 show water velocities (U) and driving forces (T) as a function of the wing chord length (c) when the natural frequencies (f_n) of scaled up systems are assumed to be 0.5, 1, 1.67 and 2 *Hz*. Re exceeds a critical Reynolds number of 3.7×10^5 around approximately $T = 1000$ *N* for any frequency, while c at which Re reaches the

critical Reynolds number varies for each frequency. c becomes about 190, 135, 105 and 95 *mm* for f = 0.5, 1, 1.67 and 2 *Hz*, respectively. Diaphragm-type DE generators with a DE diameter of 80 *mm* have the generation performance of 0.49 *N/mm* and 0.8 *mJ/mm* per unit stroke as shown in Figure 2.11. If the maximum allowable stroke of the DE generators is 12 *mm*, this system is capable of being equipped with up to approximately 170 units of the DE generator and generating electric energy of about 1.6 *J* per unit stroke. The scaled-up system equipped with the 170 units of the DE generator can be expected to generate electric power of approximately 3.3 *W* with a wing chord length of 95 *mm* and a water velocity of 1.9 *m/s* for a frequency of 2 *Hz*.

From these results, we can expect that our system is capable of supplying power to street lumps on a bridge and remote sensing devices for fatigue crack of a bridge using Karman vortices in the wake of the bridge piers.

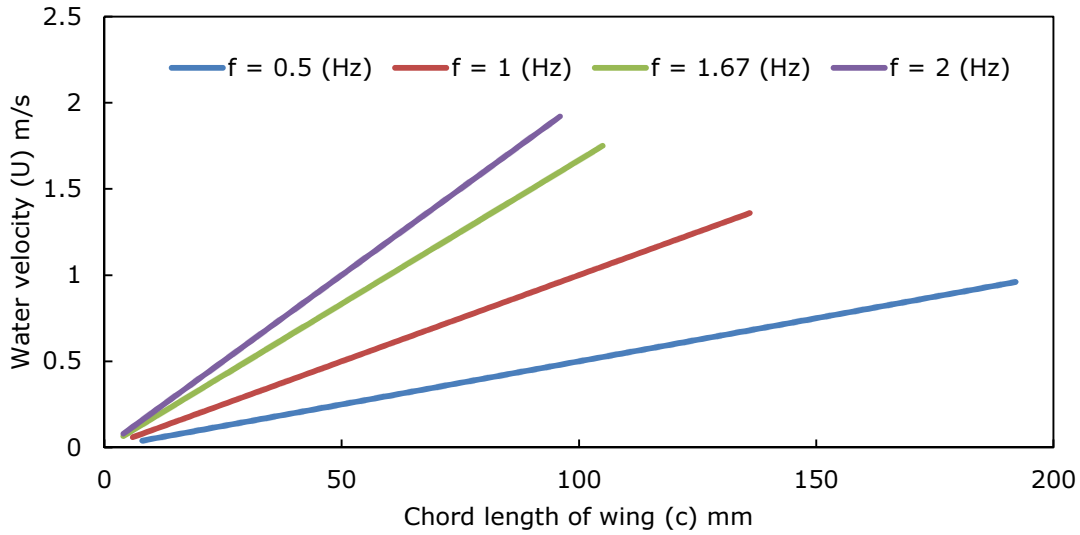

Figure 3.13 Water velocity (U) as a function of chord length of wing (c).

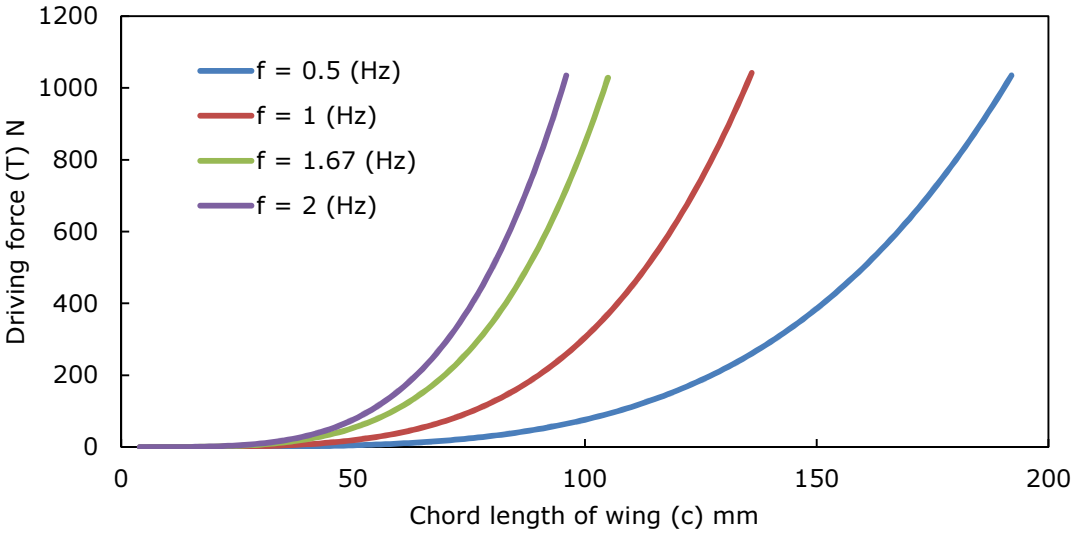

Figure 3.14 Driving force (T) as a function of chord length of wing (c).

CHAPTER 4

EXPERIMENTAL MEASUREMENTS OF DRIVE CHARACTERSISTICS AND FLOW FIELDS OF THE SYSTEM

We focused on the oscillation of the wing that is directly associated with the generation performance in the proposed system. The drive characteristics of the wing and the flow fields around the wing were measured in a small circulating water channel.

4.1 Measurements of Drive Characteristics in Small Circulating Water Channel

4.1.1 Measuring Apparatus

The wing oscillation amplitude (a) is measured with a laser displacement sensor (IL-600, Keyence Corp.) as shown in Figure 4.1.

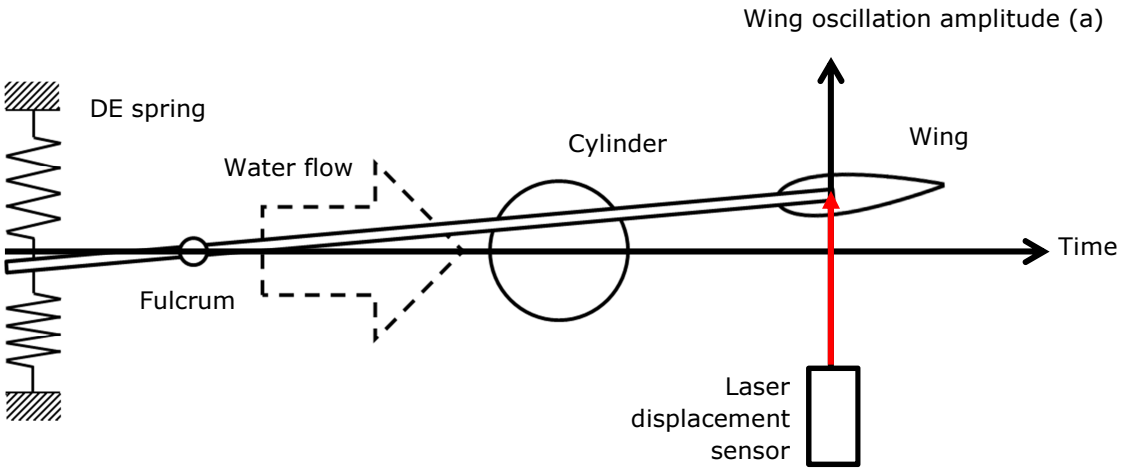

Figure 4.1 Measurement of the wing oscillation amplitude (a) with a laser displacement sensor.

4.1.2 Test Conditions

The experimental model fabricated in Chapter 3 was used. The property of the experimental model and the test conditions are summarized in Table 4.1.

Table 4.1 Parameters of the experimental model and test conditions.

Wing shape	NACA0021
Chord length of wing (c)	30 *mm*
Span length of wing (s)	120 *mm*
Distance between fulcrum to cylinder (l_{fc})	370 *mm*
Distance between DE springs to fulcrum (l_{sf})	100 *mm*
Distance between cylinder to wing (l_{cw})	100, 140, 160, 170, 180, and 200 *mm*
Diameter of cylinder (D)	48, 60, 76 *mm*
Water velocity (U)	0.30 to 0.70 *m/s* by 0.05 *m/s*

4.1.3 Results and Discussion

Figure 4.2 shows an example of measured time history result for a cylinder diameter of D = 60 *mm*, a distance between the cylinder and the wing of l_{cw} = 160 *mm*, and a water velocity of U = 0.5 *m/s*. Fast Fourier Transform (FFT) is performed for each time history of the wing vibration amplitude (a) to acquire frequency characteristics of the wing oscillations. As shown in Figure 4.3, the wing oscillates with an amplitude of about a = 9.1 mm and a frequency of about f = 1.8 *Hz* for D = 60 *mm*, l_{cw} = 160 *mm*, and U = 0.5 *m/s*.

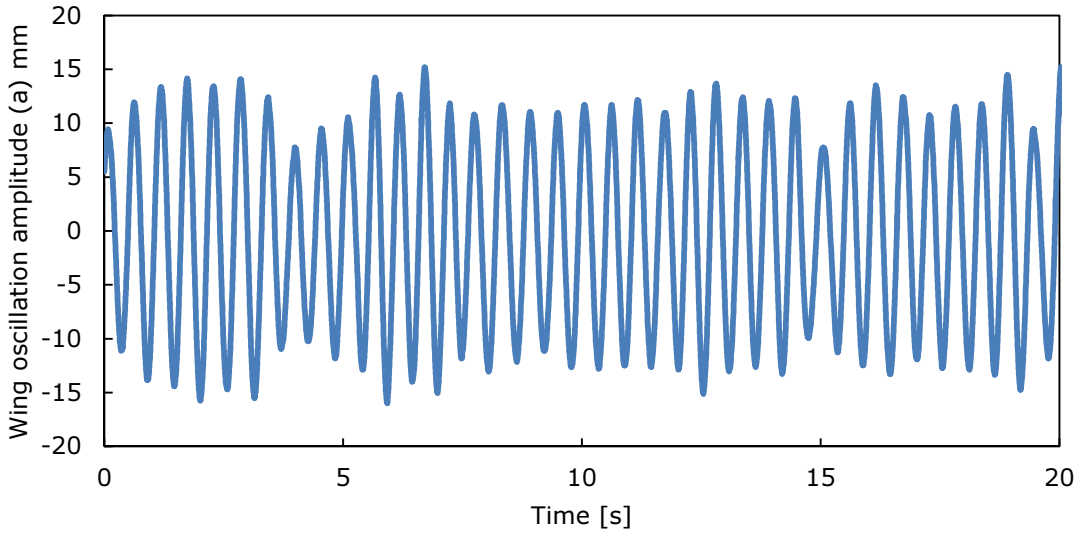

Figure 4.2 Example of measuring result for a cylinder diameter of D = 60 *mm*, a distance between the cylinder and the wing of l_{cw} = 160 *mm*, and a water velocity of U = 0.5 *m/s*.

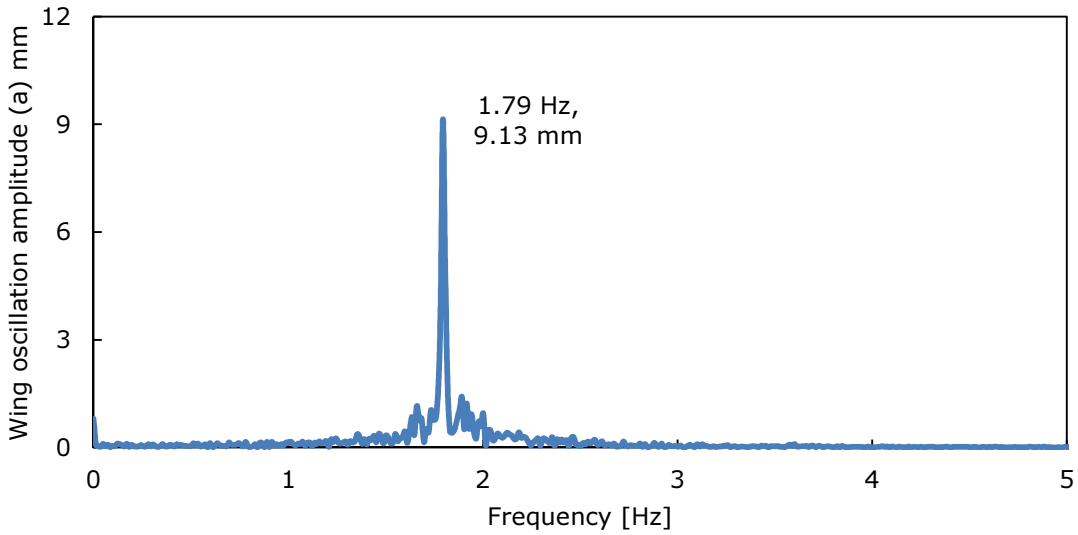

Figure 4.3 The wing oscillation amplitude (a) as a function of frequency for D = 60 *mm*, l_{cw} = 160 *mm*, and U = 0.5 *m/s*.

Now, non-dimensional parameters of the present system are considered to compare with each result. Non-dimensional amplitude (a/D) is ratio between the oscillation amplitude (a) and the cylinder diameter (D), and also non-dimensional distance between the cylinder and the wing (l_{cw}/D) is obtained by dividing l_{cw} by D. Reduced velocity (U_r) is the non-dimensional velocity and defined as :

$$U_r = \frac{U}{f_n D} \tag{4.1}$$

where f_n is the natural frequency. The natural frequency at each l_{cw} shown in Table 4.4 has been measured by averaging several free vibration tests as shown in Figure 4.4.

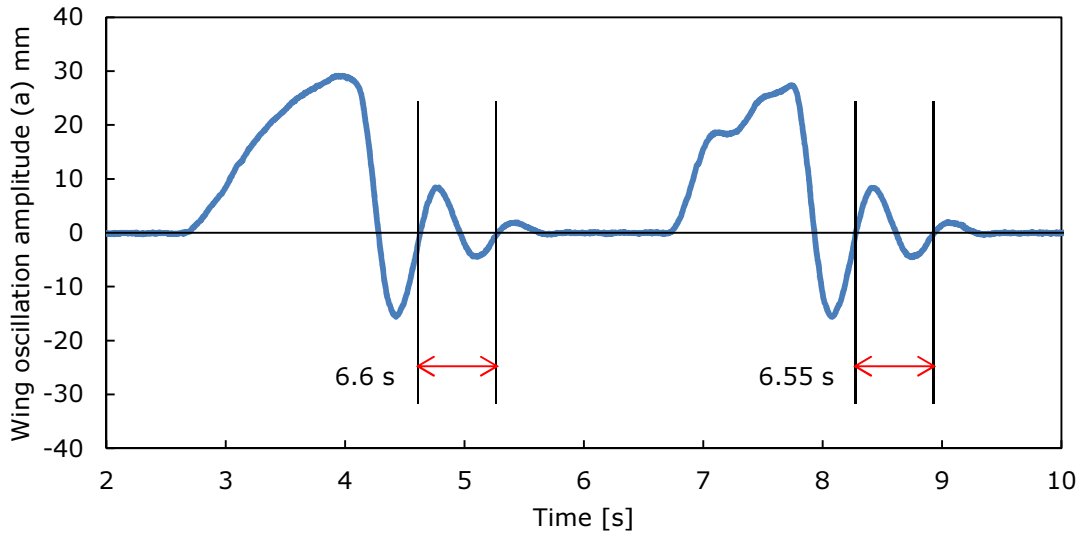

Figure 4.4 Example of free vibration test for a distance between the cylinder and the wing of l_{cw} = 200 *mm*.

Table 4.2 The natural frequency (f_n) of the fabricated model.

Distance between the cylinder and the wing (l_{cw}) *mm*	100	140	160	170	180	200
Natural frequency (f_n) *Hz*	1.73	1.64	1.61	1.59	1.59	1.52

In addition, non-dimensional frequency (f/f_n) is ratio between the vibration frequency (f) and the natural frequency (f_n), and non-dimensional chord length (c/D) is ratio between the chord length of the wing (c) and the cylinder diameter (D).

Figures 4.5-4.7 show the ratio between the wing vibration frequency (f) and the vortex shedding frequency (f_v) obtained from Equation 2.5 as a function of reduced velocity (U_r) for non-dimensional chord lengths of c/D = 0.625, 0.5 and 0.395, respectively. The wing vibration frequency agrees very well with the vortex shedding frequency from these figures. Therefore, the wing vibration is found to be driven by Karman vortices.

For c/D = 0.625 shown in Figure 4.5, however, the values of f/f_v vary and become slightly smaller than those for c/D = 0.5 and 0.395 shown in Figures 4.6 and 4.7, respectively. This is because the diameter of the cylinder (D) is small relative to the chord length of the wing (c), resulting in generation of Karman vortices with a small scale for the wing. Furthermore, the vortices are considered to be dissipated by viscosity before they reach the wing because the wing is relatively distant from the cylinder.

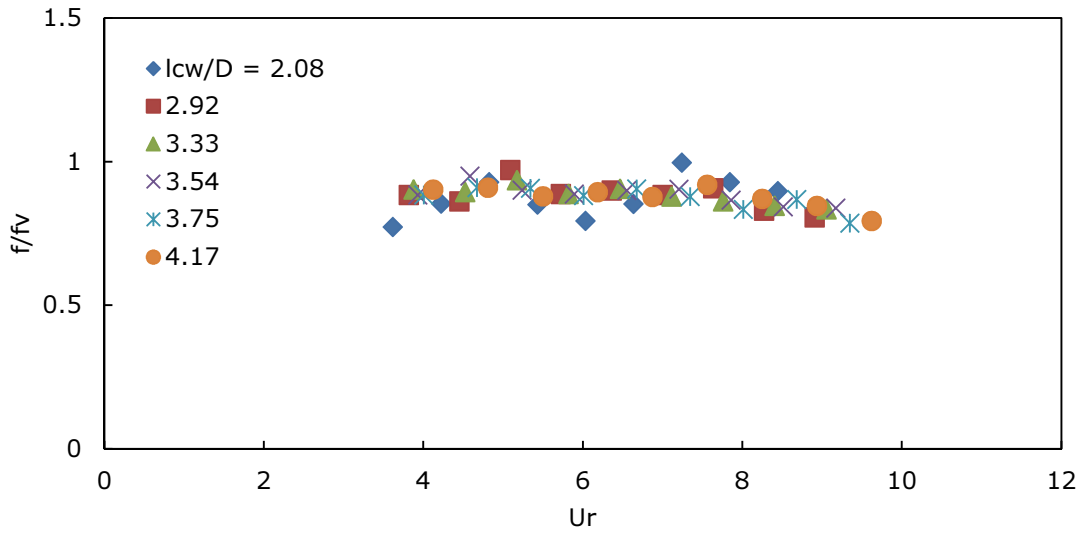

Figure 4.5 Ratio between the wing vibration frequency (f) and the vortex shedding frequency (f_v) as a function of reduced velocity (U_r) for a non-dimensional chord length of c/D = 0.625.

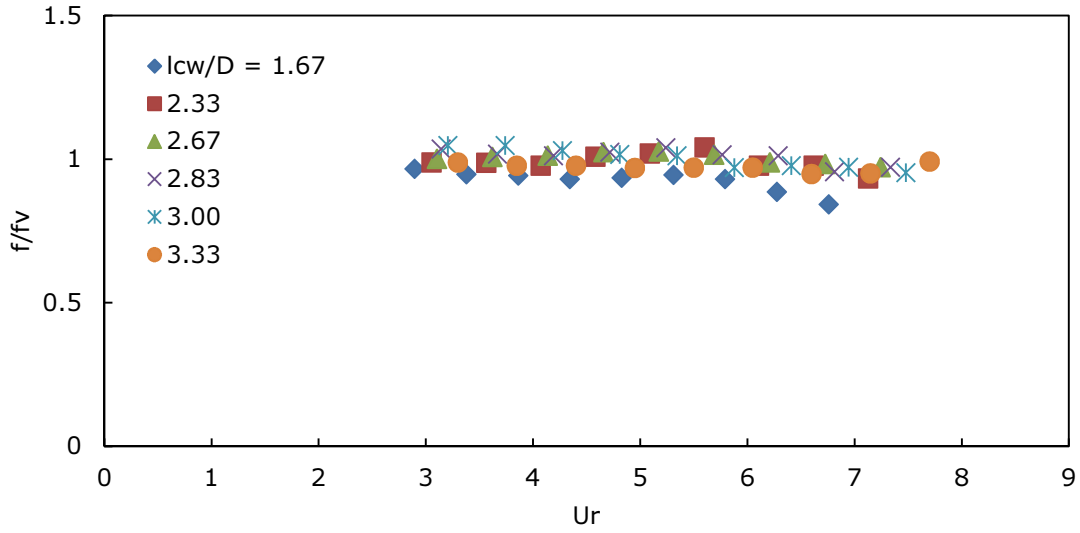

Figure 4.6 Ratio between the wing vibration frequency (f) and vortex shedding frequency (f_v) as a function of reduced velocity (U_r) for a non-dimensional chord length of $c/D = 0.5$.

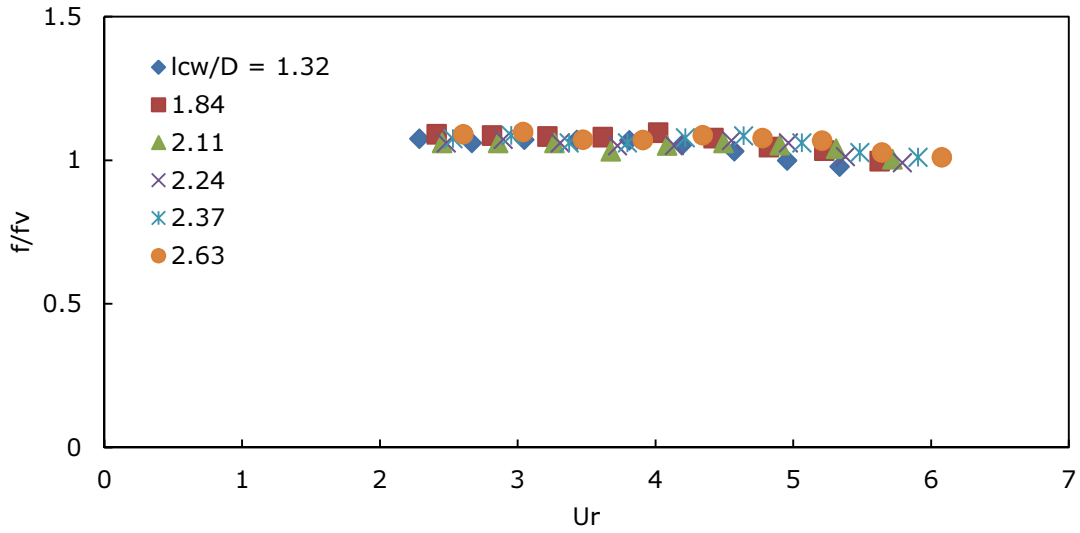

Figure 4.7 Ratio between the wing vibration frequency (f) and vortex shedding frequency (f_v) as a function of reduced velocity (U_r) for a non-dimensional chord length of $c/D = 0.395$.

Figures 4.8-4.10 show the non-dimensional frequency (f/f_n) as a function of reduced velocity (U_r) for non-dimensional chord lengths of c/D = 0.625, 0.5 and 0.395, respectively. As the reduced velocity (U_r) increases, f/f_n increases. f/f_n becomes 1 for around U_r = 5, which means the resonance point.

Since $f \approx f_v$ from Figures 4.5-4.7, $f_n \approx f_v$ is obtained for f/f_n = 1. Using this and Equation 4.1, the reduced velocity (U_r) can be written in the form:

$$U_r = \frac{U}{f_n D} \approx \frac{U}{f_v D} \tag{4.2}$$

The third side of Equation 4.2 is found to be the reciprocal of the Strouhal number (St) defined in Equation 2.5. Hence the following equation is obtained:

$$U_r = 1/St \tag{4.3}$$

Because St is experimentally found to be approximately equal to 0.21 in $500 < Re < 3.7\times10^5$ where Re is the Reynolds number defined by Equation 2.4 for circular cylinders [21], U_r becomes about 5 for f/f_n = 1.

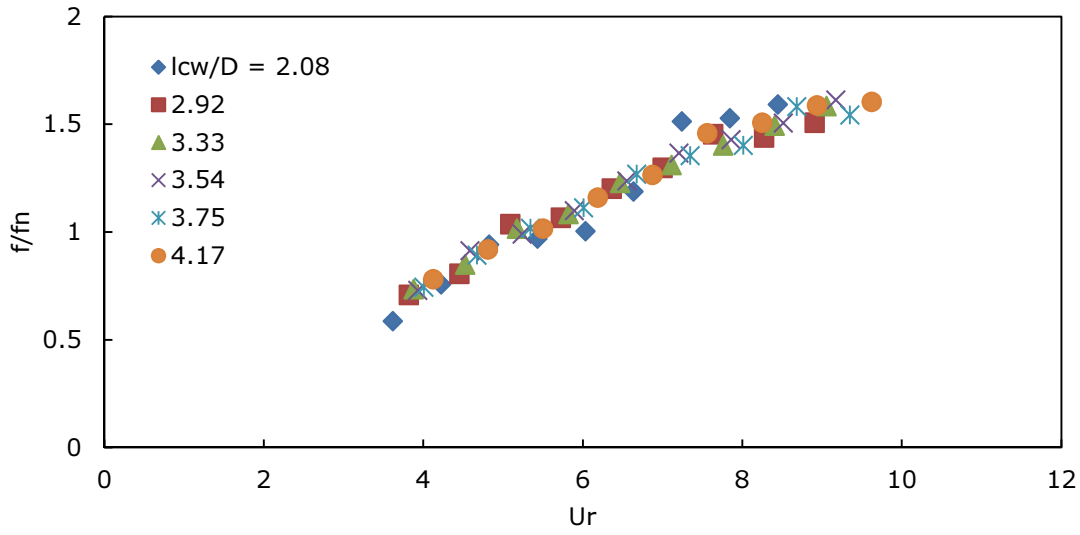

Figure 4.8 Non-dimensional frequency (f/f_n) as a function of reduced velocity (U_r) for a non-dimensional chord length of $c/D = 0.625$.

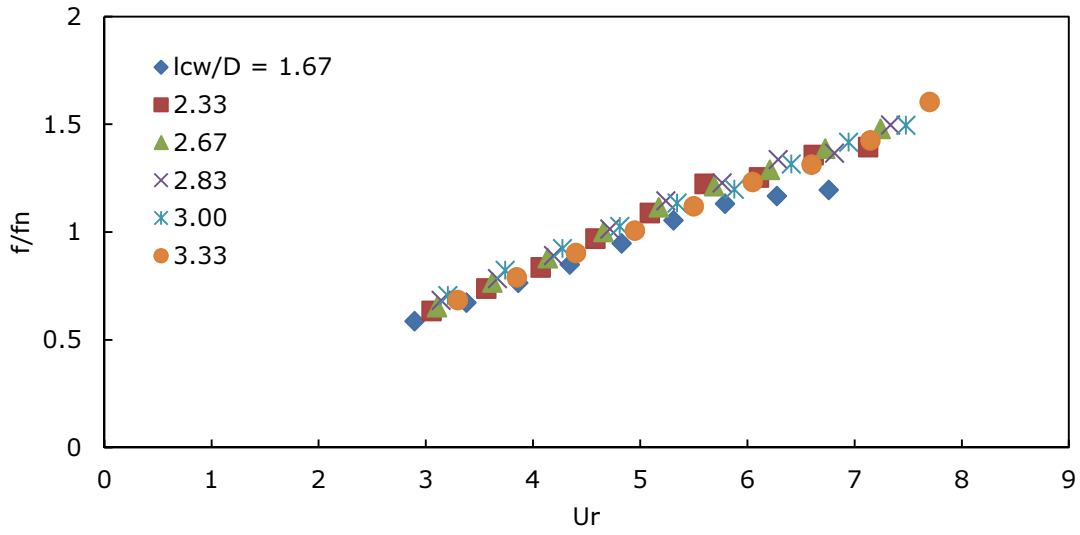

Figure 4.9 Non-dimensional frequency (f/f_n) as a function of reduced velocity (U_r) for a non-dimensional chord length of $c/D = 0.5$.

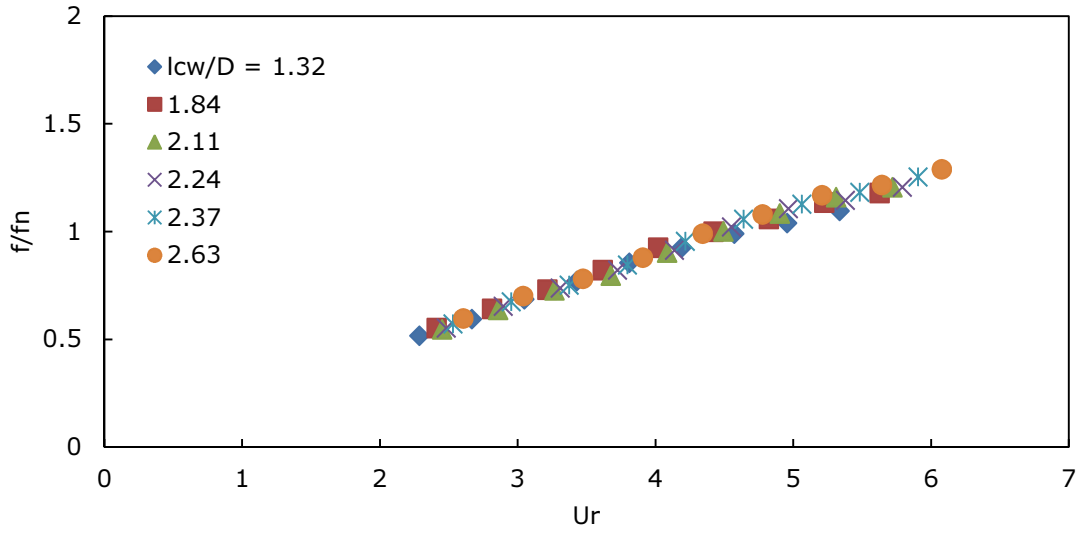

Figure 4.10 Non-dimensional frequency (f/f_n) as a function of reduced velocity (U_r) for a non-dimensional chord length of c/D = 0.395.

Figures 4.11-4.13 show the non-dimensional amplitude (a/D) as a function of reduced velocity (U_r) for non-dimensional chord lengths of c/D = 0.625, 0.5 and 0.395, respectively. Although a/D becomes larger because of the resonance effect for U_r = 5 in Figure 4.12 and Figure 4.13, a/D becomes largest for U_r = 6.5 and relatively small in Figure 4.11. Moreover, when U_r and l_{cw}/D become about 5 and 2.6, respectively, the maximum of a/D is obtained for c/D = 0.5 and 0.395.

As shown in Figure 4.5, the wing oscillation frequency (f) becomes slightly small relative to the vortex shedding frequency (f_v) obtained by Equation 2.5 for c/D = 0.625. Accordingly, the denominator of the third side of Equation 4.2 decreases and U_r increases. Also, a/D for c/D = 0.625 becomes very small compared to c/D = 0.5 and 0.395 because the wing is large relative to the cylinder and relatively distant from the cylinder, which means Karman vortices become a smaller scale for the wing and are dissipated by viscosity before they reach the wing.

From the results for c/D = 0.5 shown in Figure 4.12, the values of a/D around U_r = 5, which are the resonance amplitude, are found to vary widely according to the

non-dimensional distance between the cylinder and the wing (l_{cw}/D). For l_{cw}/D = 1.67, a/D becomes very small because Karman vortices are considered to be not fully developed near the cylinder. a/D shows larger amplitude in the range of 2.33 < l_{cw}/D < 3. When l_{cw}/D becomes 3.33, a/D decreases again owing to dissipation of vorticity by viscosity probably.

As a consequence, large oscillation amplitude of the wing can be obtained at the reduced velocity of approximately U_r = 5, the non-dimensional distance between the cylinder and the wing of approximately l_{cw}/D = 2.67 and the non-dimensional chord length of c/D > 0.625.

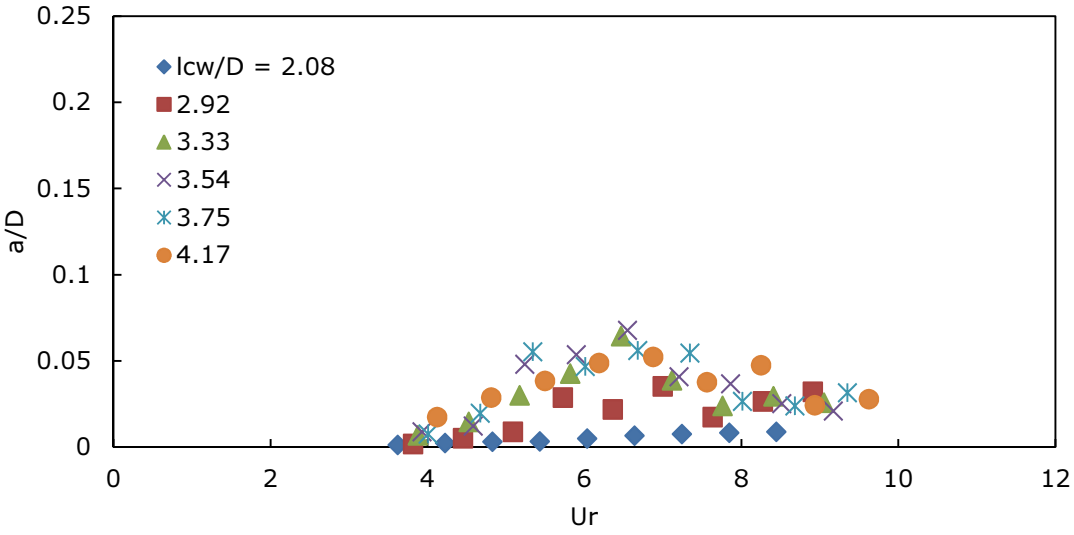

Figure 4.11 Non-dimensional amplitude (a/D) as a function of reduced velocity (U_r) for a non-dimensional chord length of c/D = 0.625.

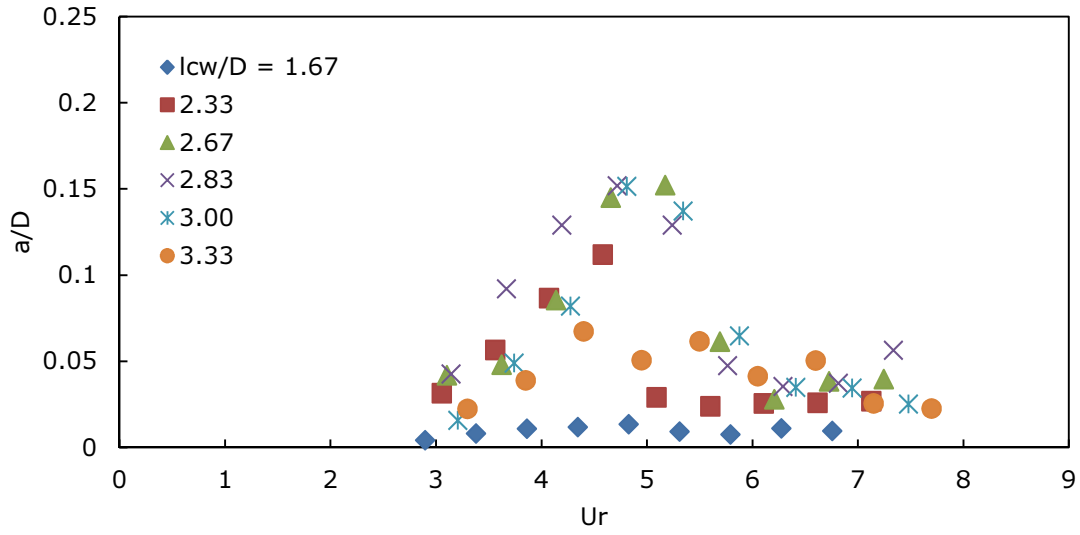

Figure 4.12 Non-dimensional amplitude (a/D) as a function of reduced velocity (U_r) for a non-dimensional chord length of $c/D = 0.5$.

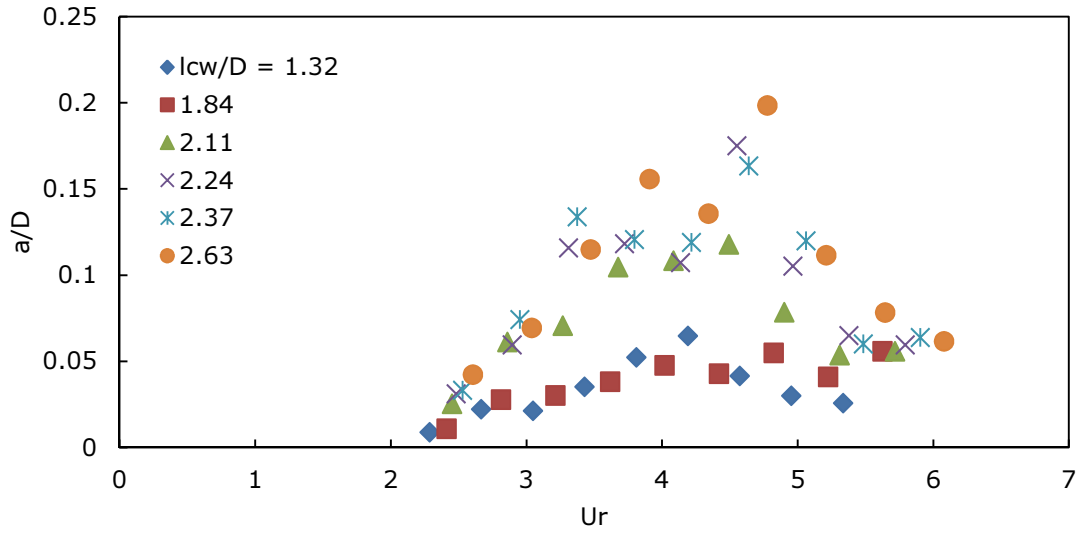

Figure 4.13 Non-dimensional amplitude (a/D) as a function of reduced velocity (U_r) for a non-dimensional chord length of $c/D = 0.395$.

4.2 Flow Fields Measured by PIV analysis

4.2.1 Flow Visualization and PIV analysis

Particle Image Velocimetry (PIV) analysis is carried out by the a PIV software (nexus PIV 2000, Nexus Inc.) to measure the flow pattern around the wing. As shown in Figure 4.14, the optical system is set for PIV analysis. Laser light, which is emitted from a laser source (VA-I-SLM-532, Beijing Viasho Technology Co., Ltd.), is transformed into laser light sheet through a cylindrical lens. A half mirror and mirrors are used as that the laser light sheet is irradiated from both sides of the wing to prevent shadows of the wing. Tracer particles (DIAION HP20SS, Mitsubishi Chemical Corp.) are recorded from below by a high-speed camera (HAS-220, DITECT Corp.). The recorded pictures are analyzed by the PIV software.

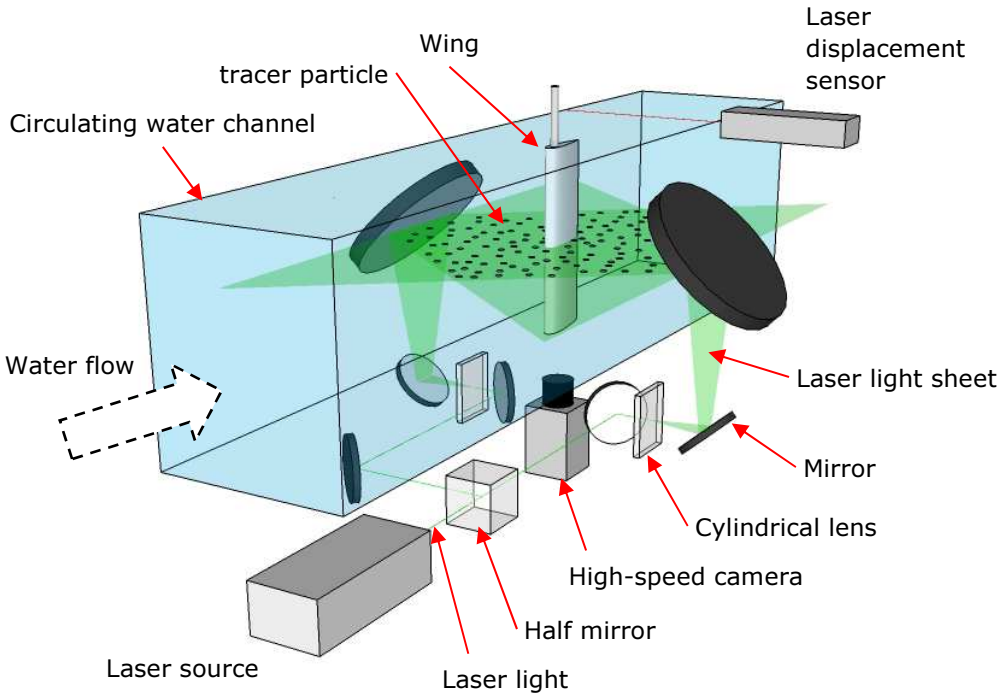

Figure 4.14 Schematic view of measuring apparatus.

4.2.3 Results and Discussion

Figure 4.15 show the flow fields around the wing obtained by PIV analysis for the distance between the cylinder and the wing (l_{cw}) of 100 *mm*, the cylinder diameter (D) of 60 *mm* (i.e., l_{cw}/D = 1.67), and the water velocity (U) of 0.5 *m/s*. Figures 4.15a-h show the half-cycle of the wing vibration with 8 pictures. Directions of the vectors in the diagrams indicate the flow direction and lengths of the vectors indicate magnitude of the flow velocity. The wing is located in the center of the diagrams and there is no vectors on the wing. The vectors around the wing have very small length and various directions, which means a dead water region having a complicated flow field around l_{cw}/D = 1.67. This is the reason why the wing oscillation amplitude becomes very small at l_{cw}/D = 1.67 as shown in Figure 4.12. We can also observe that a strong flow streams into the middle of the channel around the right side in the diagrams. Therefore, Karman vortices are considered to be fully developed around l_{cw}/D = 2.67.

Figure 4.16 show the flow fields around the wing by PIV analysis for the distance between the cylinder and the wing (l_{cw}) of 160 *mm*, the cylinder diameter (D) of 60 *mm* (i.e., l_{cw}/D = 2.67), and the water velocity (U) of 0.5 *m/s*. Figures 4.16a-h also show the half-cycle of the wing vibration with 8 pictures. Under this condition, the wing oscillation amplitude becomes larger as shown in Figure 4.12. A strong flow is found to stream toward the wing obviously from the diagrams, resulting in large oscillation amplitude of the wing. Positional relation between the wing and vortices will be discussed in Chapter 5.

In comparison with Figure 4.15 and Figure 4.16, we can observe that vortices which drive the wing are not fully developed near the cylinder owing to a dead water region. It is important to set the wing at the non-dimensional distance between the cylinder and the wing of approximately l_{cw}/D = 2.67 for larger oscillation amplitude.

(a) $t = 0$ [s]

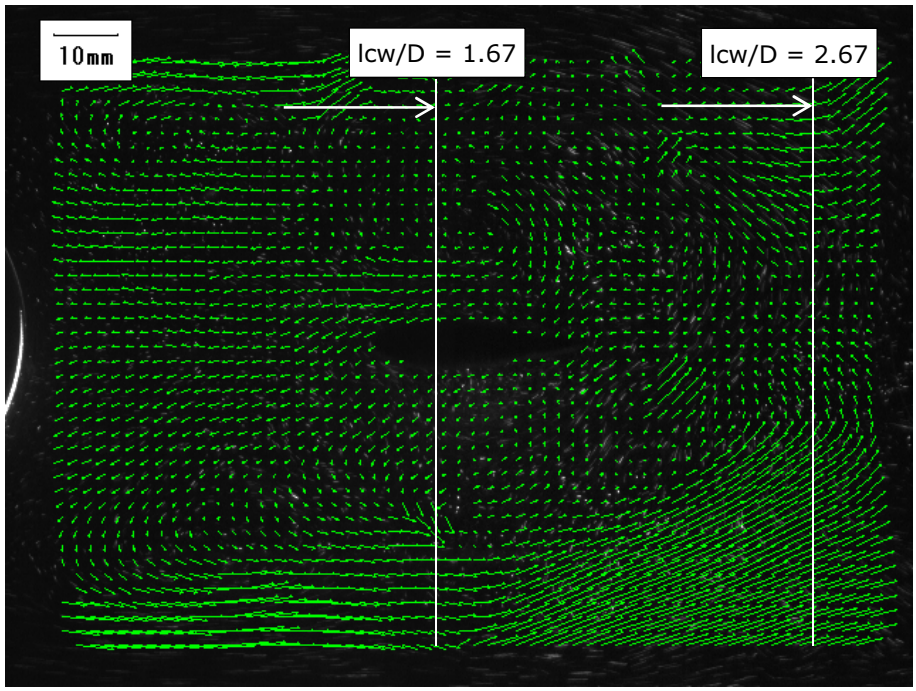

(b) $t = (1/14)T$ [s]

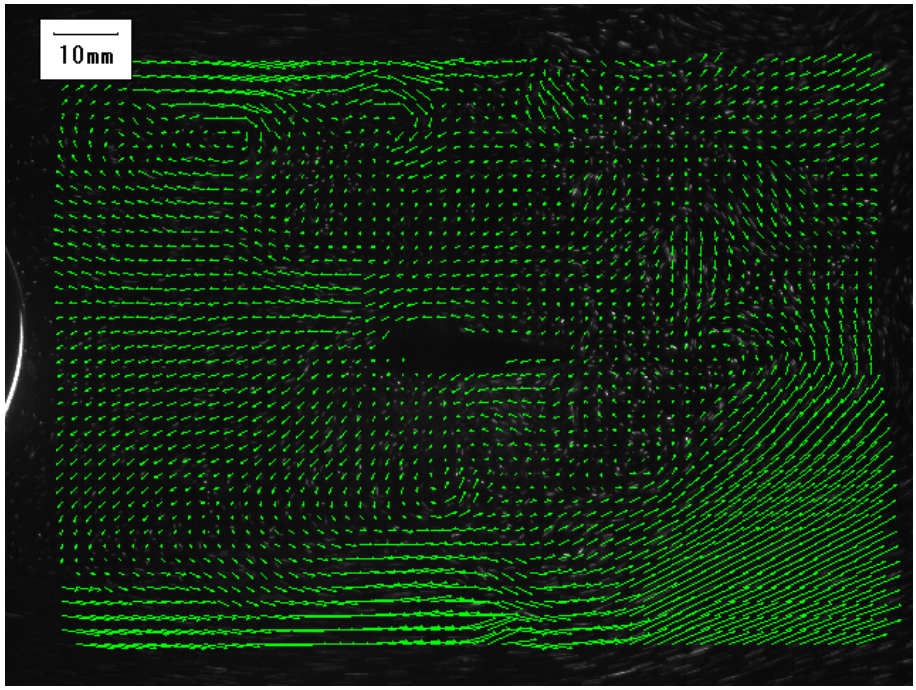

Figure 4.15 Flow fields around the wing by PIV analysis for the distance between the cylinder and the wing (l_{cw}) of 100 *mm*, the cylinder diameter (D) of 60 *mm* (i.e., $l_{cw}/D = 1.67$), and the water velocity (U) of 0.5 *m/s*.

(c) $t = (1/7)T$ [s]

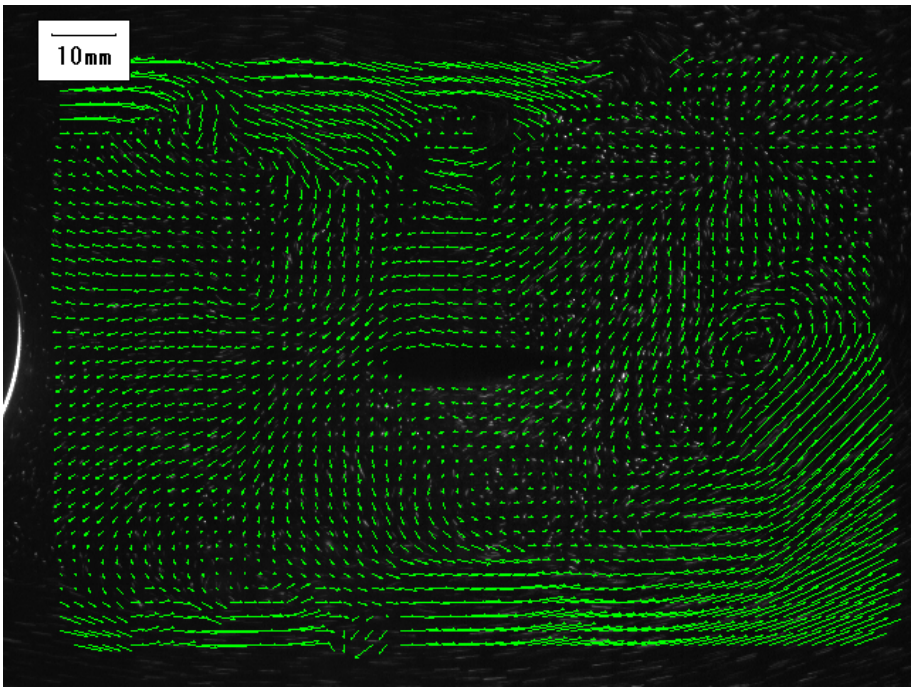

(d) $t = (3/14)T$ [s]

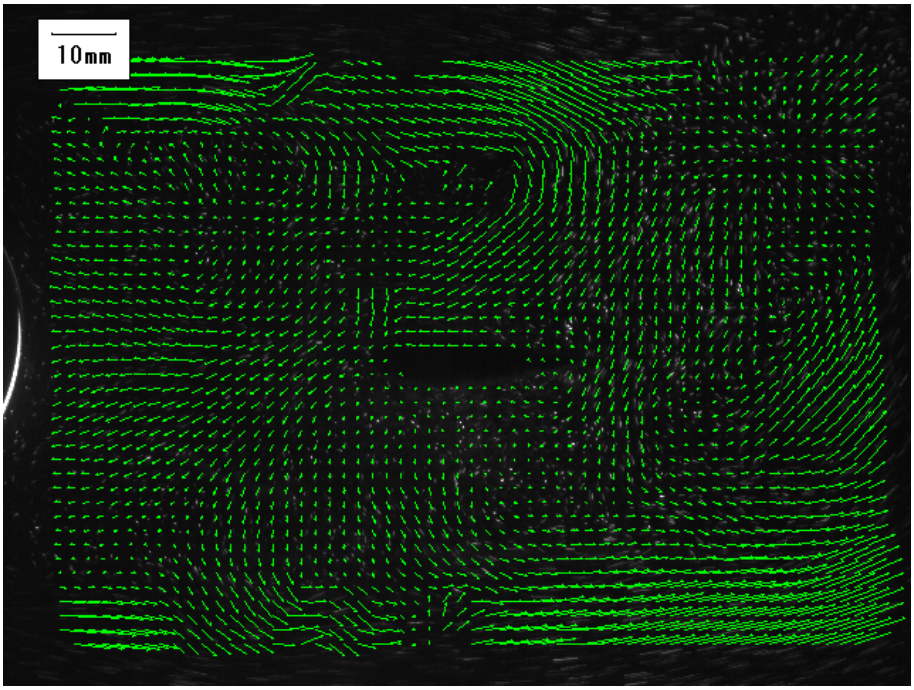

Figure 4.15 (Continued).

(e) $t = (2/7)T$ [s]

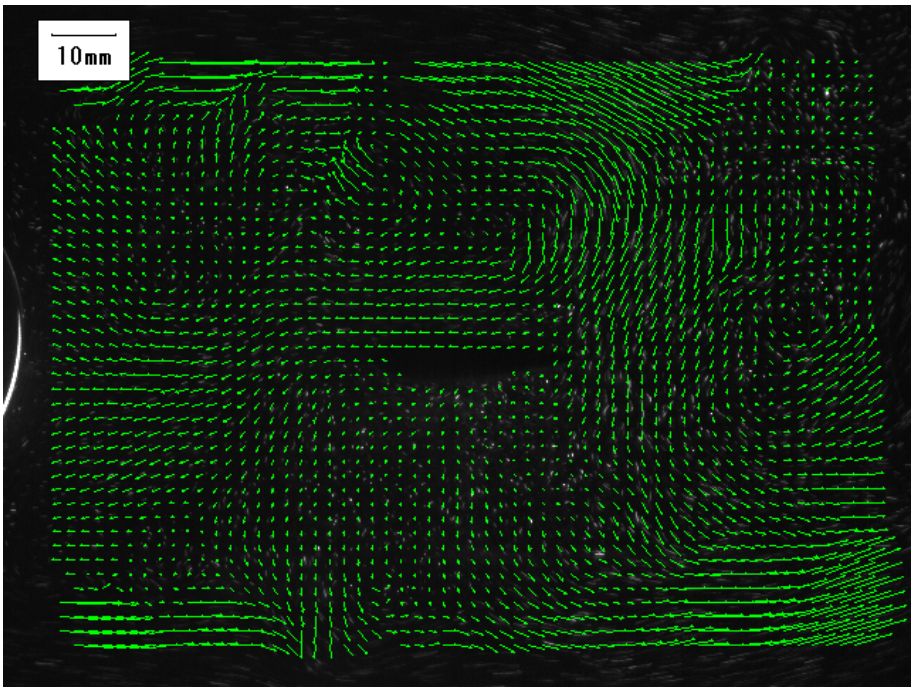

(f) $t = (5/14)T$ [s]

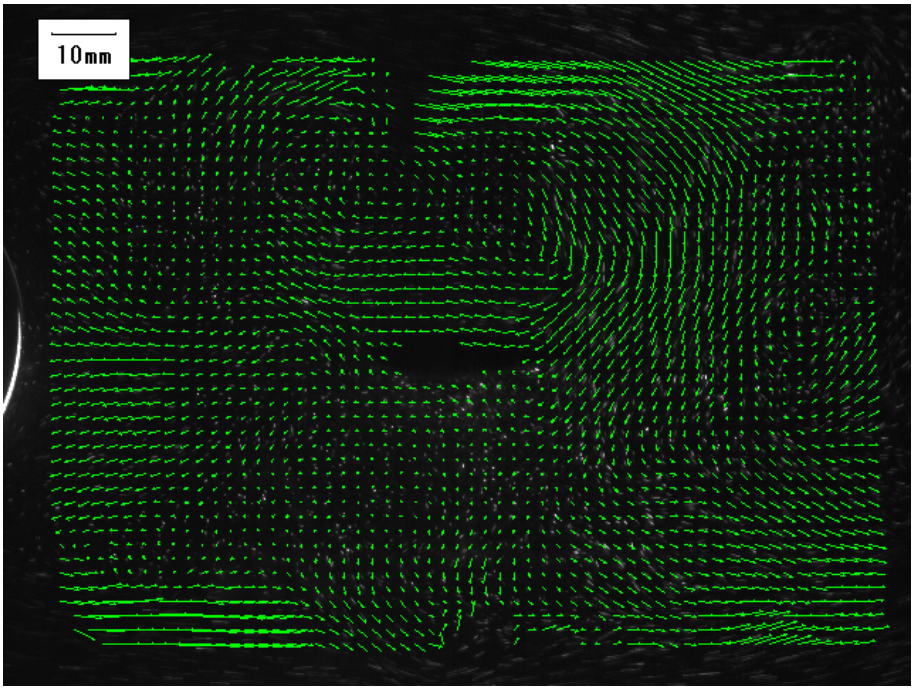

Figure 4.15 (Continued).

(g) $t = (3/7)T$ [s]

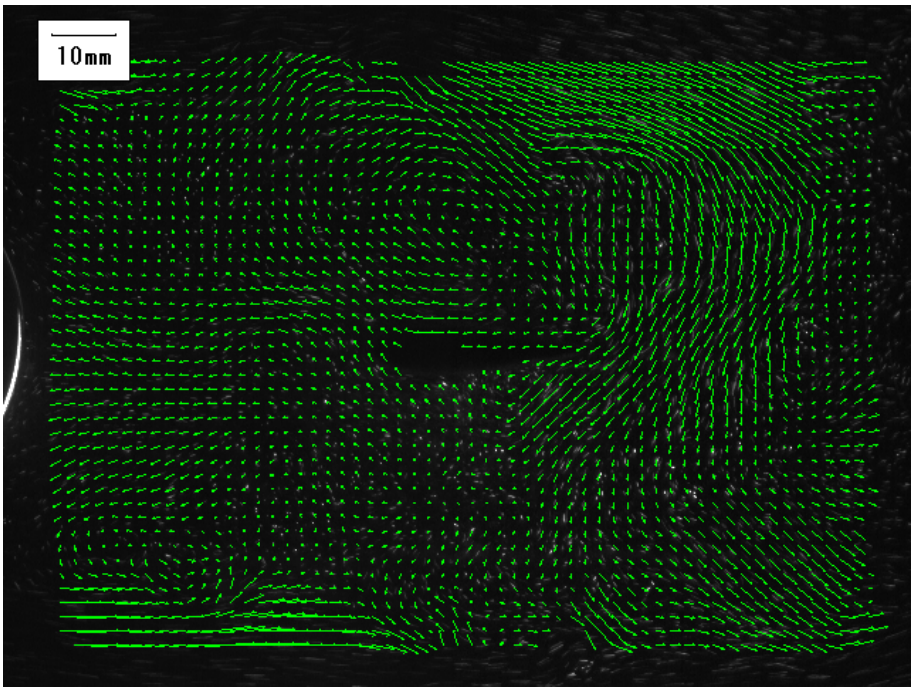

(h) $t = (1/2)T$ [s]

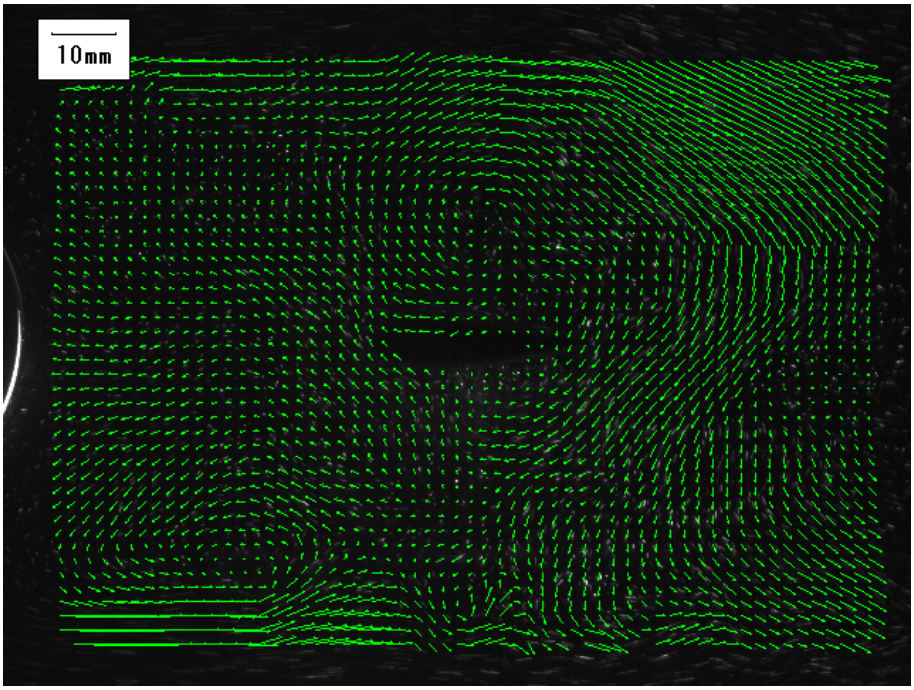

Figure 4.15 (Continued).

(a) $t = 0$ [s]

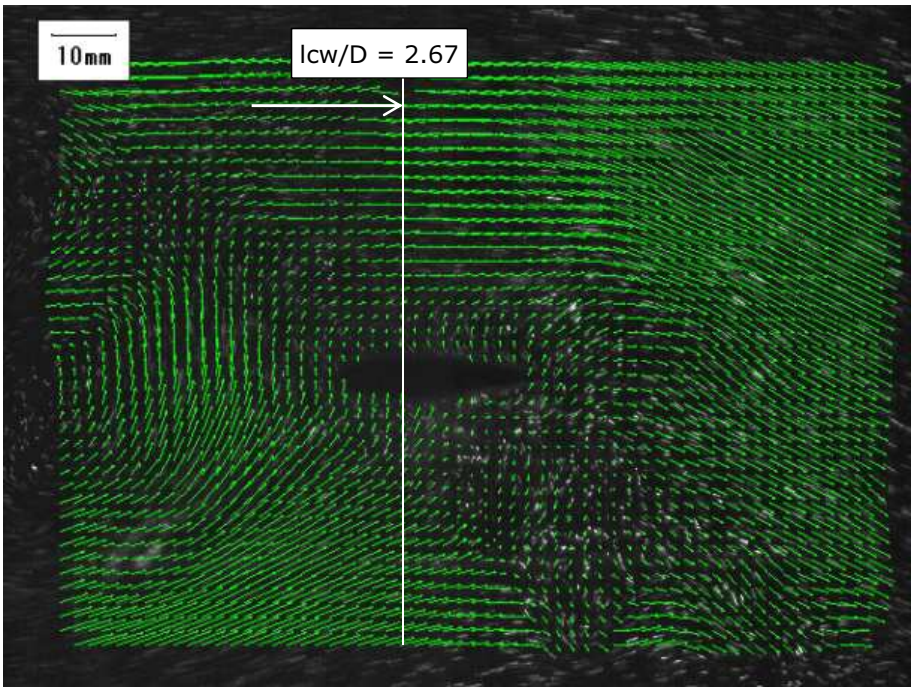

(b) $t = (1/14)T$ [s]

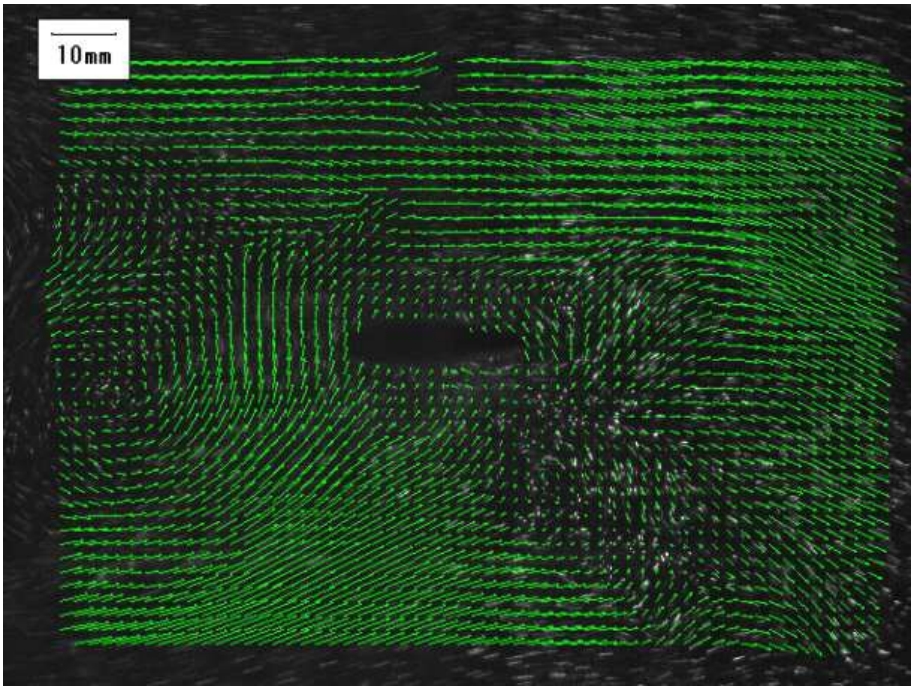

Figure 4.16 Flow fields around the wing by PIV analysis for the distance between the cylinder and the wing (l_{cw}) of 160 *mm*, the cylinder diameter (D) of 60 *mm* (i.e., $l_{cw}/D = 2.67$), and the water velocity (U) of 0.5 *m/s*.

(c) $t = (1/7)T$ [s]

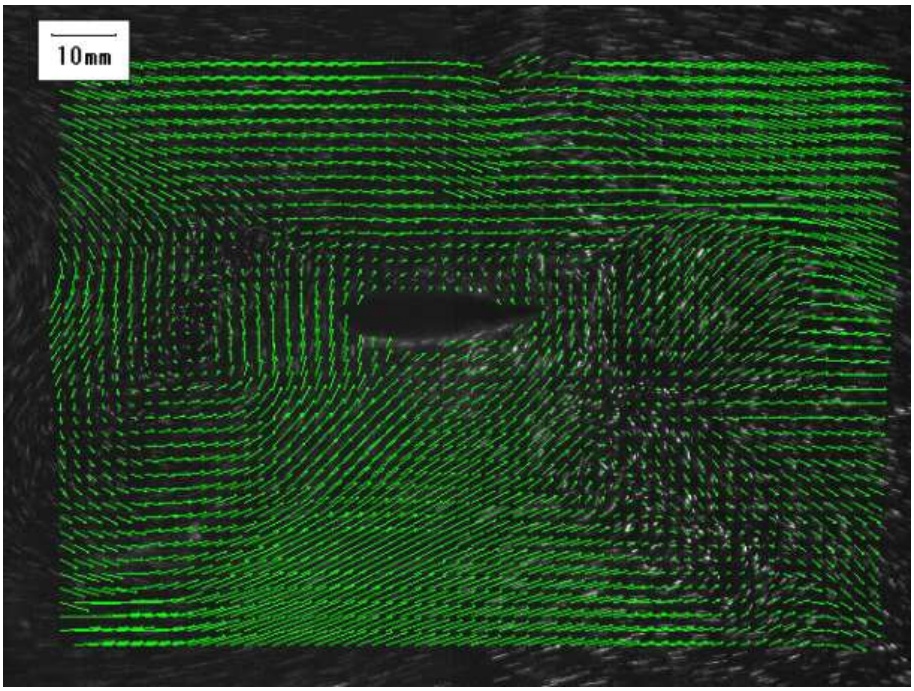

(d) $t = (3/14)T$ [s]

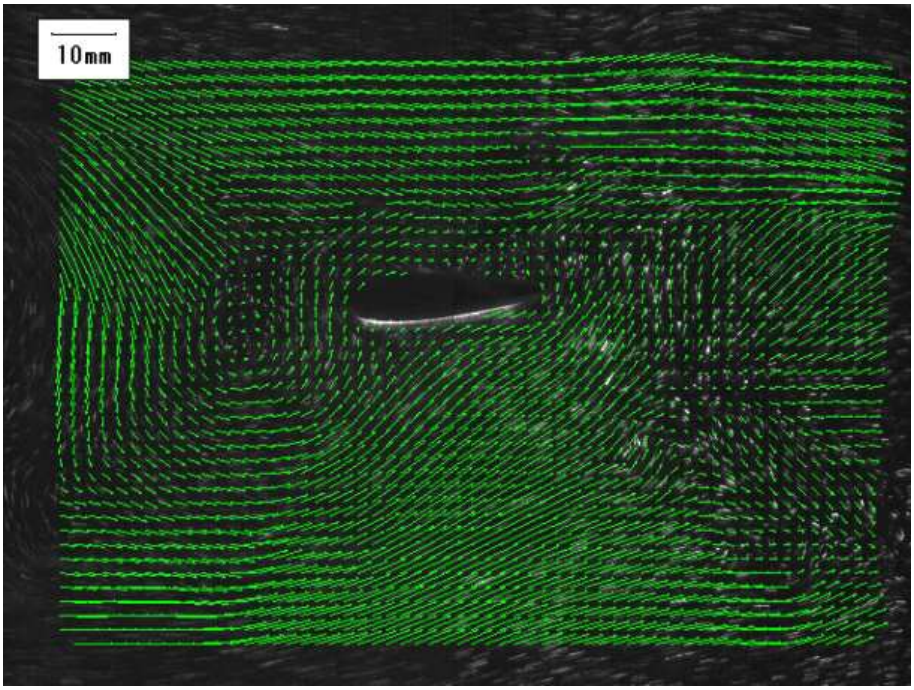

Figure 4.16 (Continued).

(e) $t = (2/7)T$ [s]

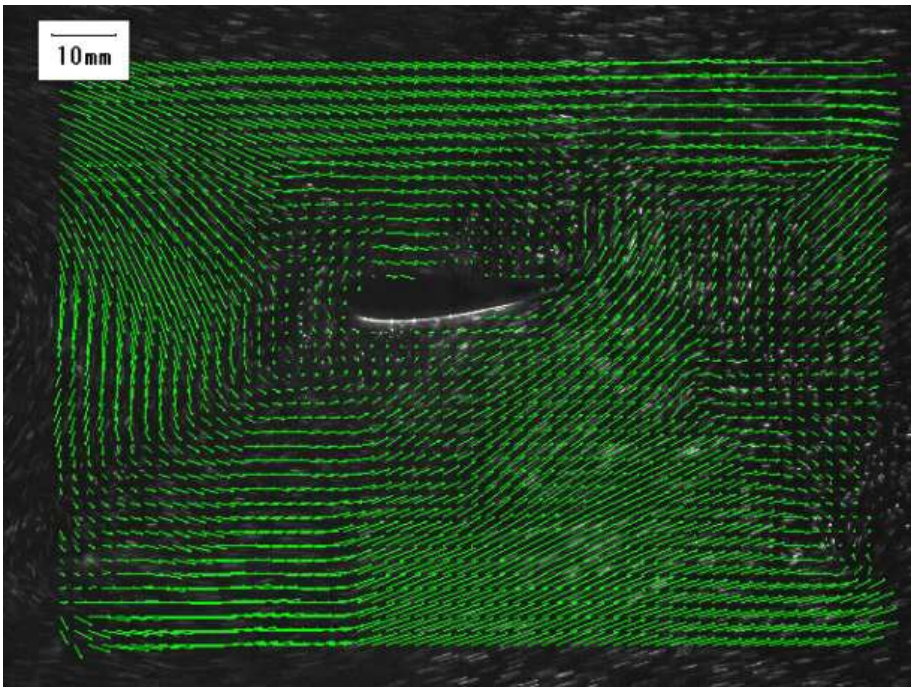

(f) $t = (5/14)T$ [s]

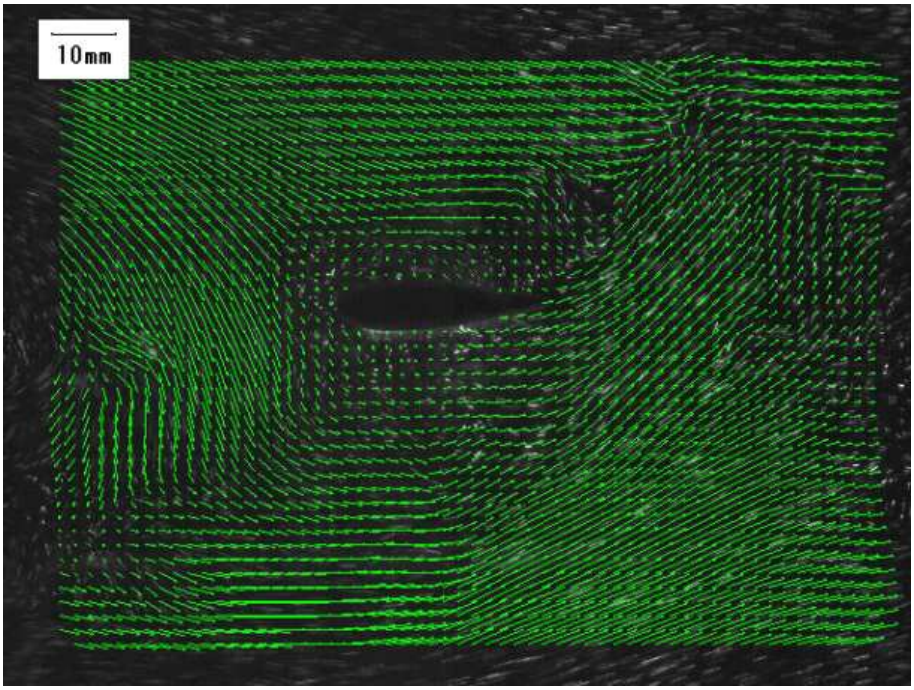

Figure 4.16 (Continued).

(g) $t = (3/7)T$ [s]

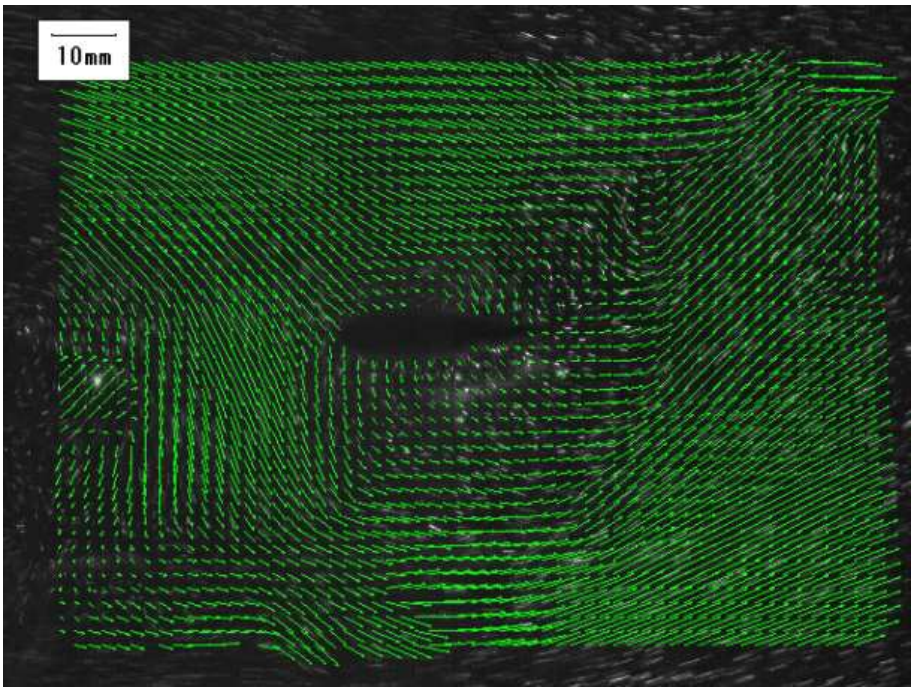

(h) $t = (1/2)T$ [s]

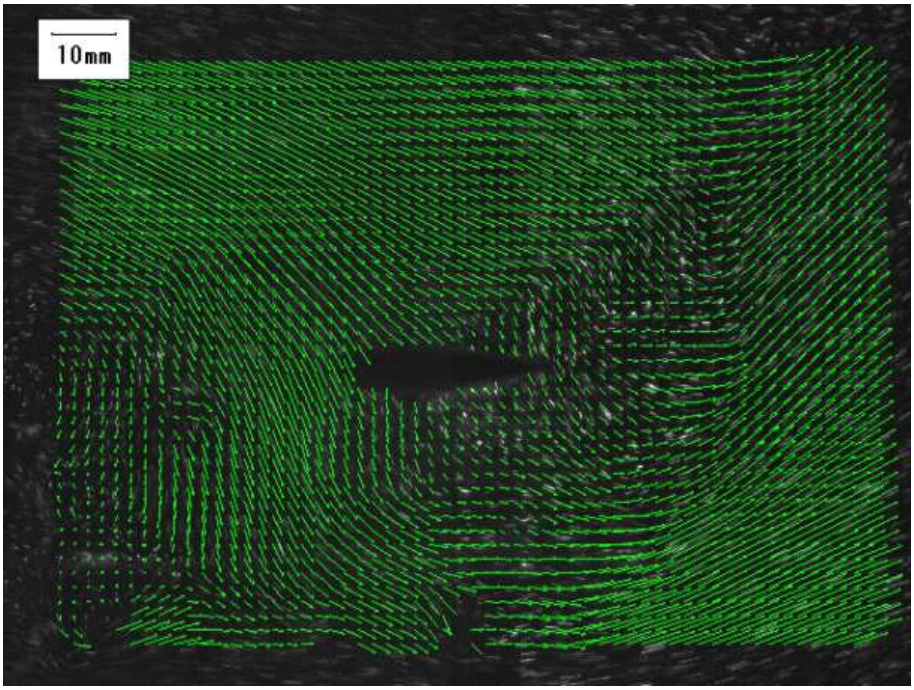

Figure 4.16 (Continued).

CHAPTER 5

PERFORMANCE EVALUATION OF THE POWER GENERATING SYSTEM BY CFD SIMULATIONS

Two-dimensional CFD analysis was carried out for the small hydropower generation system proposed in this study to evaluate its generation performance in a wide range of parameters. The wing oscillations behind a circular cylinder which generates Karman vortices ware simulated and the results were compared with the experimental data.

5.1 Computational Method

5.1.1 Flow Solver

As a flow solver, the incompressible URANS (Unsteady Reynolds Averaged Navier-Stokes) solver, SURF [29], which has been developed at National Maritime Research Institute is adopted. SURF is based on a finite volume method for unstructured grid and it has the capability of handling unsteady body motions (EoMs) implicitly coupled with a flow field are solved at each time step. Note that flows are assumed to be laminar and no turbulence model is adopted in the present computations. This is because Reynolds number are not high (1.8E+4 maximum) and because present flow fields are strongly unsteady due to the vortex shedding at a circular cylinder surface and current turbulence models cannot be expected to capture characteristics of such unsteady flows properly. Actually, the preliminary trial computation with a turbulence model did not produce reasonable results.

5.1.2 Motion Solver

In the present study, the wing moves with one degree of freedom, i.e., the rotation around the rotation axis which is set to 370 *mm* in front of the center of the cylinder. Therefore, the EoM is expressed as:

$$\frac{I}{4\rho U^2 c^3}\ddot{\theta} + \frac{K}{4\rho U^2 c^3}\theta = C_{mz} \tag{5.1}$$

where θ is the rotation angle and C_{mz} is the non-dimensional hydrodynamic moment defined as:

$$C_{mz} = \frac{M_z}{\rho U^2 c^3} \tag{5.2}$$

where M_z is the hydrodynamic moment computed by the flow solver, ρ is the water density, U is the water velocity and c is the chord length of the wing. Therefore, the left-hand of Equation 5.1 is similarly divided by $\rho U^2 c^3$. I and K are the moment of inertia and the torsion spring constant, respectively. Dampers are not installed in the experiment and in the CFD computation because of very small damping force of DE generators. Damping effect due to fluid viscosity, however, is calculated in the flow solver and considered in the right-hand of Equation 5.1. It is noted that I and K are a quarter as large as the experimental values, since the span length of the wing in the simulation model is a quarter as long as the wing used in the experiment.

From the result of the simulation, the time histories of the wing oscillation amplitude (a) is obtained using Equation 5.3:

$$a = \left(l_{fc} + l_{cw}\right)\sin\theta \tag{5.3}$$

where l_{fc} and l_{cw} are the length between the rotation axis and the cylinder center and the length between the cylinder center and a quarter-chord of the wing.

5.2 Simulation Design

5.2.1 Test Cases

Two-dimensional flow analysis are carried out with water velocities (U) of 0.4, 0.5 and 0.6 m/s, i.e., Reynolds number (Re) of 11,952, 14,940 and 17,928.

5.2.2 Grids and Boundary Conditions

Computational grids are generated by the commercial software Pointwise and they consist of blocks of hexahedra cells. An overview of the grid and the boundary conditions are shown in Figure 5.1a. As the boundary conditions, no slip wall (wing an cylinder walls), inflow, outflow, and free slip wall (channel walls) are utilized. The computational domain has a length of 107c (-51.0 $\leq x/c \leq$ 56.0) and a width of 10c (-5,0 $\leq y/c \leq$ 5.0) where the origin of the coordinates is set at the center of the cylinder. At x = -51.0c, the inflow boundary condition is applied. The outflow and the free slip wall boundary conditions are similarly applied at x = 56.0c and y = ±5.0c, respectively. The width corresponds to that of the circulating water channel used in the experiment. The cylinder and the wing locate at $x/c \leq$ 1.0 and 5.0 $\leq x/c \leq$ 6.0, respectively, in the computational domain. A rotation axis is set to 12.3c in front of the cylinder (Figure 5.1b). The total number of cells (N) is 11,520 and the smallest grid spacing normal to the wall is set to 7.0E-5c.

As for the mesh dependency, comparison of averaged rotation angles for cases with different numbers of cells is shown in Table 5.1. The differences from the current grid (N = 11,520) are considered acceptable on account of unsteady and nonlinear natures of

the current model. Since the channel width is relatively small compared with a cylinder, there may be a blockage effect. However, this is out of scope of the current paper, which is the comparison between the experiment and CFD results with the same condition.

Table 5.1 Mesh dependency.

Total number of cells	9,856	11,520	14,848
Error of rotation angle [%]	1.7	-	9.0

(a)

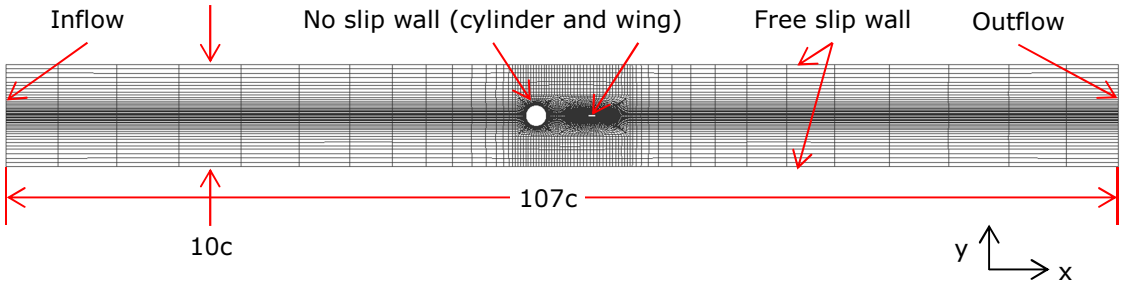

(b)

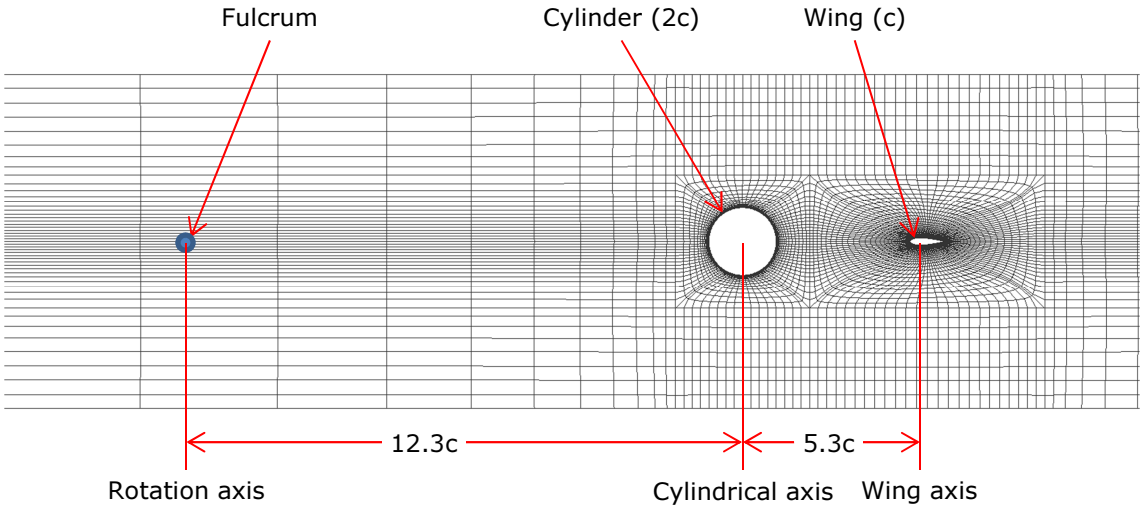

Figure 5.1 (a) Grid overview and boundary conditions, (b) enlarged view around the cylinder and the wing.

5.3 Results and Discussion

5.3.1 Drive Characteristics

Figures 5.2-5.4 show the comparison between CFD analysis and experimental results of the wing oscillations for each Reynolds number (*Re*). The time histories of the wing oscillation amplitude (*a*) are shown in Figures 5.2a-5.4a. Fast Fourier Transform (FFT) is performed for each time history of *a* to acquire frequency characteristics of the wing oscillations (Figure 5.2b-5.4b).

When the water velocity (*U*) is 0.4 *m/s* (i.e., *Re* = 11,952), the experimental result mainly consists of the oscillation having a frequency (*f*) of about 1.37 *Hz* and an amplitude (*a*) of about 8.0 *mm*. For the CFD result, *f* is about 1.63 *Hz* and *a* is about 2.6 *mm* (Figure 5.2). When *U* becomes 0.5 *m/s* (*Re* = 14,940), the experimental result shows the oscillation with the dominant *f* of about 1.76 *Hz* and a of about 12.0 *mm*. The oscillation of the CFD result has *f* of about 2.03 *Hz* and *a* of about 6.5 *mm* (Figure 5.3). For *U* = 0.6 *m/s* (*Re* = 17,928), the wing oscillation of the experimental results yields small amplitude which is about 2.9 *mm* with *f* of about 2.00 *Hz*. On the other hand, the CFD result shows large amplitude of about 11.8 *mm* and *f* of about 2.44 *Hz* (Figure 5.4).

The wing oscillation frequencies obtained by the CFD results tend to be approximately 15% larger than the experimental results for each *Re*. Since the vortex shedding frequency (f_v) in the present study can be estimated by Equation 2.5, f_v are approximately 1.40, 1.75 and 2.10 *Hz* for *U* of 0.4, 0.5 and 0.6 *m/s*, respectively. The vortex shedding frequencies agree very well with the experimental results. In addition, the experimental results of *a* becomes the largest value of about 12 *mm* owing to resonance when f_v is close to the natural frequency of 1.61 *Hz* in the present model, i.e., *U* is 0.5 *m/s*. CFD results, however, show the peak of *a* for *U* = 0.6 *m/s*. It seems that the conversion of the moment of inertia (*I*) and the torsion spring constant (*K*) of the measurement from the three-dimensional experimental model to the two-dimensional CFD simulation model may have some effects. Also, the two-dimensional flow assumption of the simulations may yield the discrepancies of the oscillation frequencies

and of the resonance point. However, in comparison between the CFD result for $U = 0.6$ *m/*s and the experimental result for $U = 0.5$ *m/s*, both the wing oscillation amplitudes are nearly equal to each other and both can be assumed to be at the resonance point.

(a)

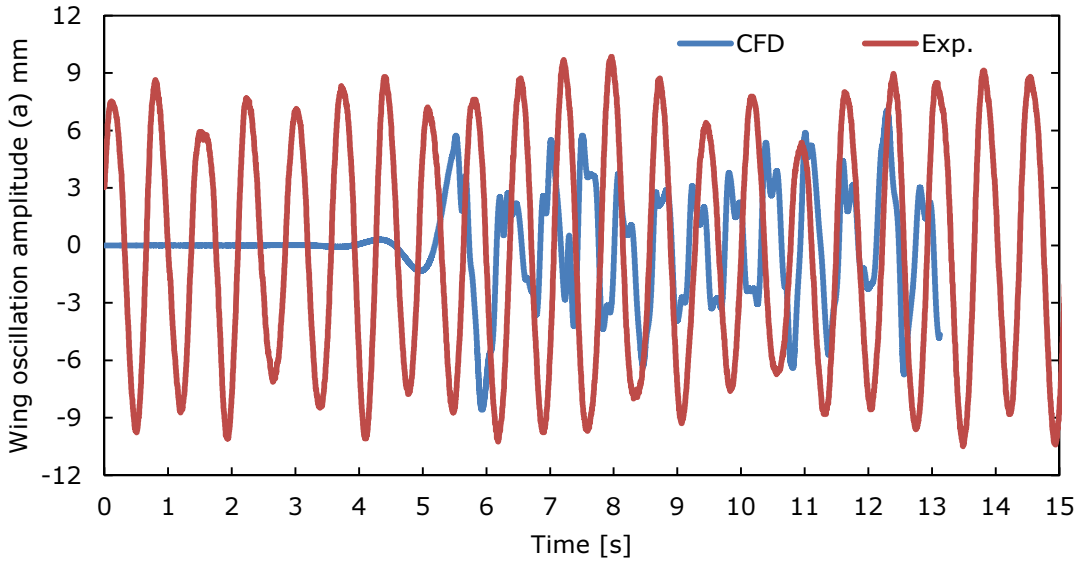

(b)

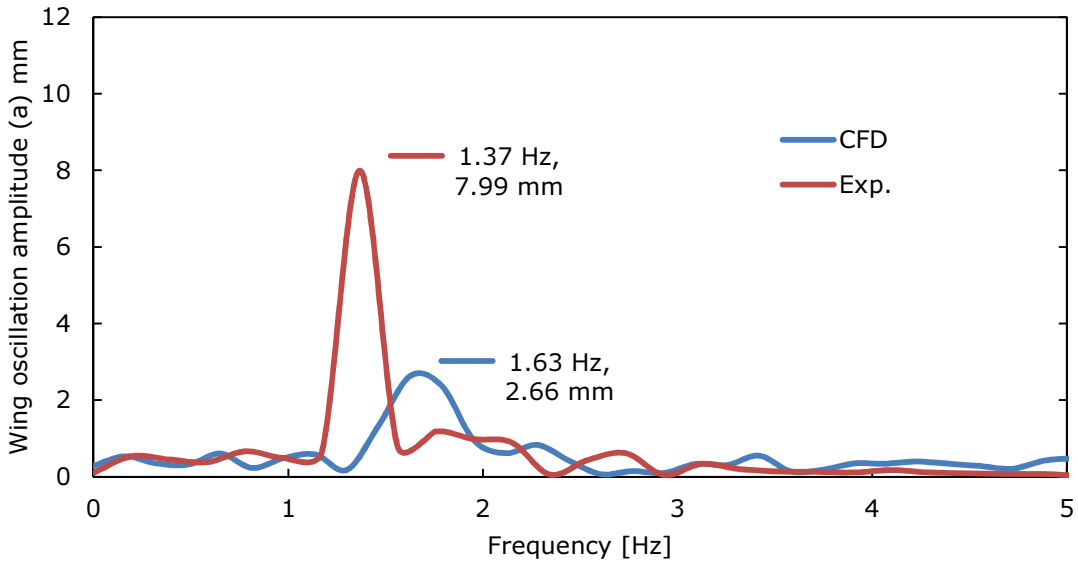

Figure 5.2 CFD and experimental results for Re = 11,952 (U = 0.4 *m/s*), (a) the time histories of the wing oscillation amplitude (a), (b) a as a function of frequency (f).

(a)

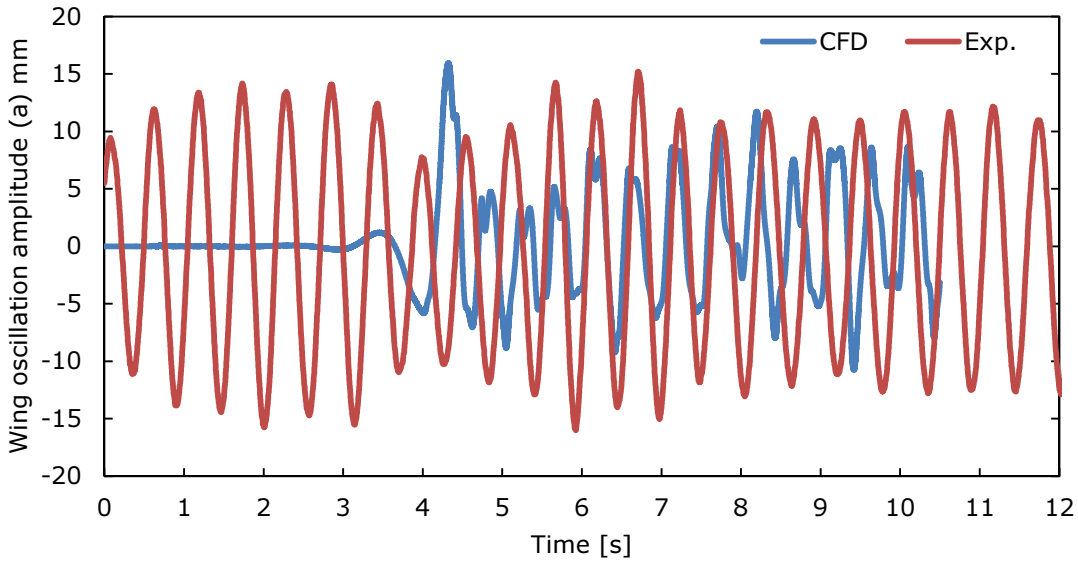

(b)

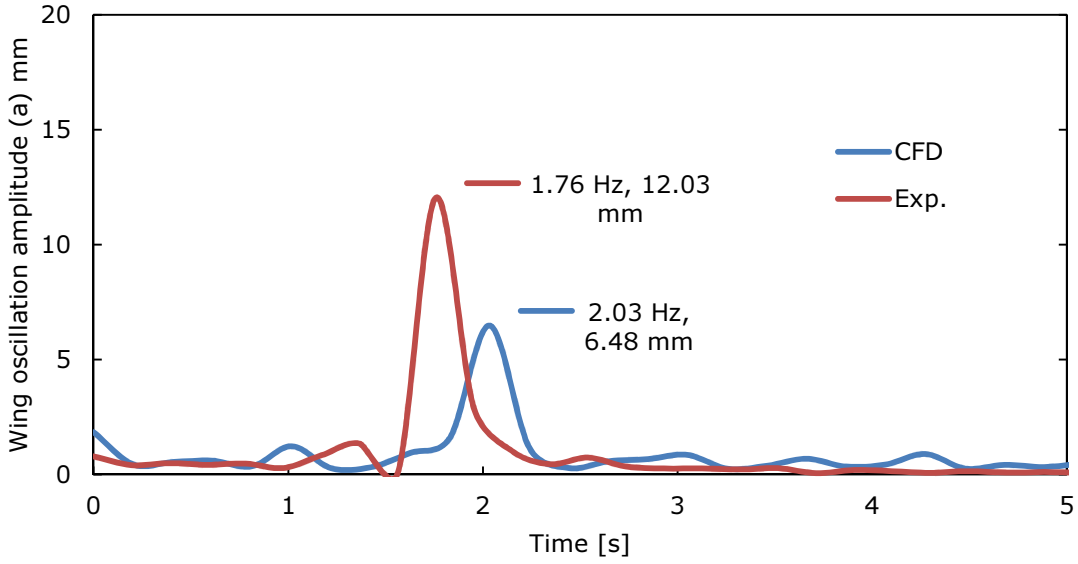

Figure 5.3 CFD and experimental results for Re = 14,940 (U = 0.5 *m/s*), (a) the time histories of the wing oscillation amplitude (a), (b) a as a function of frequency (f).

(a)

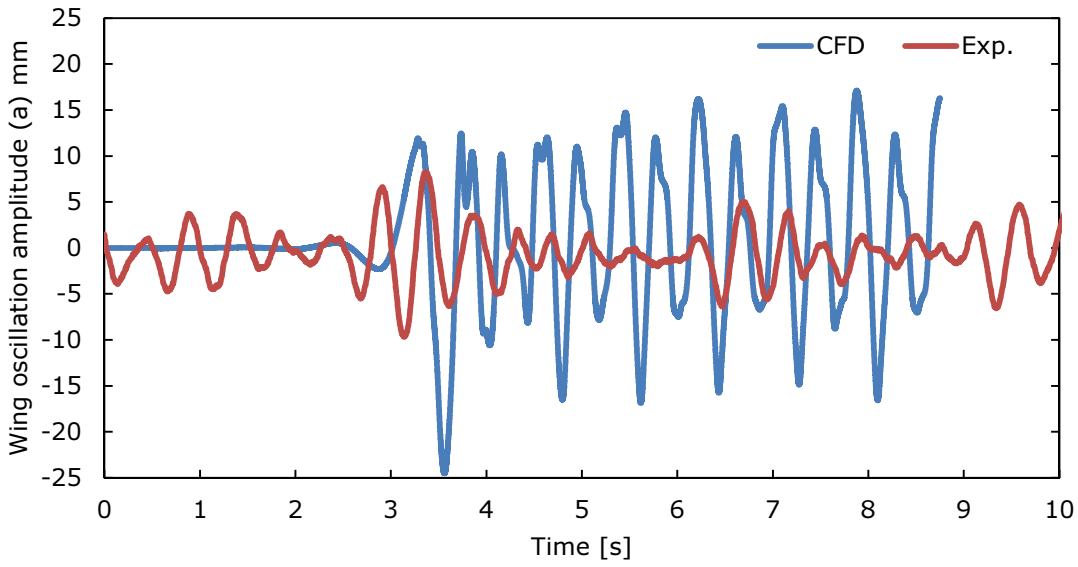

(b)

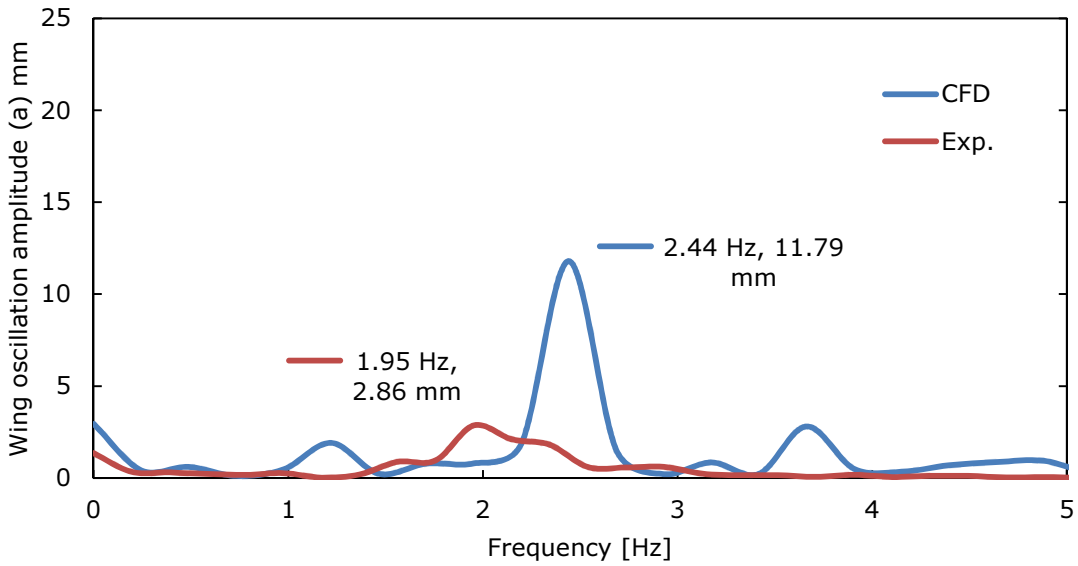

Figure 5.4 CFD and experimental results for *Re* = 17,928 (*U* = 0.6 *m/s*), (a) the time histories of the wing oscillation amplitude (*a*), (b) *a* as a function of frequency (*f*).

5.3.2 Flow Fields

Figures 5.5-5.7 show the flow fields around the wing in comparison between the CFD result of U = 0.6 *m/s* and the experimental data of U = 0.5 *m/s*, where the oscillation amplitude of the CFD result is close to the resonance amplitude of the experiment as stated above.

Figures 5.5a-5.7a present the flow fields obtained by the CFD analysis for Re = 17,928 (U = 0.6 *m/s*). Figure 5.5b-5.7b present the flow fields obtained by the PIV measurements for Re = 14,940 (U = 0.5 *m/s*). The wing position is indicated in the lower right part of each figure. Figure 5.5a, for example, shows the flow fields when the wing is near the center and moving upward. Figure 5.6a shows the flow fields when the oscillation magnitude is maximum and in Figure5.7a the wing is on the way back to the center. The background images of Figures 5.5c-5.7c and 5.5d-5.7d are the same images with Figures 5.5a-5.7a and 5.5b-5.7b, respectively.

Figures 5.5a-5.7a of CFD results correspond to Figures 5.5b-5.7b of PIV measurements, respectively, in terms of the pattern of flow and vortices formation. The several vortices shed from the cylinder are observed in the region close to the wing and their locations relative to the wing differ at each phase of the wing oscillation. Since the CFD results are obtained by two-dimensional flow analysis, stronger vortices appear in the simulation compared with the experiment.

To clearly show the positional relation between the wing and vortices, the vortices are emphasized and distinguished by using the alphabet (e.g. vortices A, B and C) as shown in Figures 5.5c-5.7c and 5.5d-5.7d. The same indices of each figure show the identical vortices. In Figure 5.5c, we can observe the four vortices which are the vortex A located upstream of the wing, the vortex B on the upside of the wing, the vortex C and the vortex D on the downside of the wing. The blue vortices and the red vortices have a clockwise direction and a counterclockwise direction, respectively. The vortex A and the vortex B are considered as a pair of Karman vortices generated by the cylinder. A strong

upward induced velocity results from the pair of Karman vortices in the middle of the vortex A and B. Meanwhile, the vortex C and the vortex D are considered to be induced by the flow separation due to the upward motion of the wing oscillation. In comparison with the experimental result shown in Figure 5.5d, the CFD result and the PIV result correspond with respect to the vortices A, B and D. the vortex C, however, is not observed in the PIV result (Figure 5.5d). This is because vortices in the actual flow tend to disappear compared to two-dimensional flow analysis owing to diffusion of vorticity in the depth direction. When the oscillation magnitude becomes maximum as shown in Figures 5.6c and 5.6d, the vortex A approaches to the wing, the vortex D flows downstream and the vortices E and F are newly formed on the upside of the wing by the flow separation due to the upward induced velocity. The vortex B of Karman vortex which is observed in Figures 5.5c and 5.5d seems to be absorbed into the vortex E. When the wing is on the way back to the center (Figures 5.7c and 5.7d), we can observe the four vortices which are the new vortex G of Karman vortex upstream of the wing, the vortex A of Karman vortex on the downside of the wing, the vortices E and F on the upside of the wing. The strong downward induced velocity by the pair of Karman vortices can be also observed both in the CFD result and in the PIV result as shown in Figures 5.7c and 5.7d. In the present system, the fluctuation of the flow induced by Karman vortices is considered essential to the wing oscillation. Although the flow situations are not exactly the same, it appears CFD simulations can reproduce the interaction of the wing motion and the surrounding vortices to some extent.

From these results, it can be concluded that the flow characteristics of the present hydropower generation system may be able to be predicted by CFD analysis with reasonable accuracy.

(a) (c)

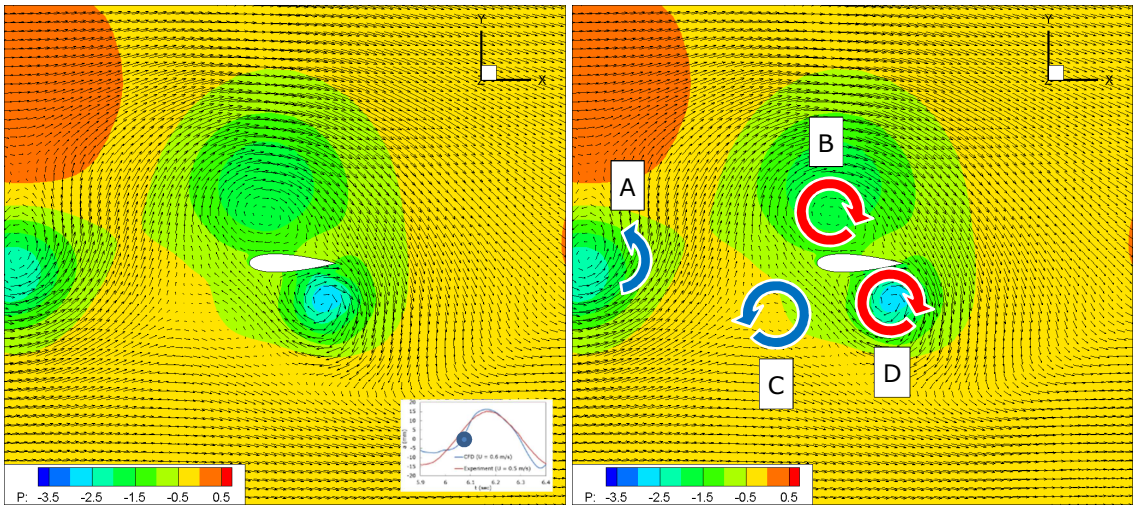

(b) (d)

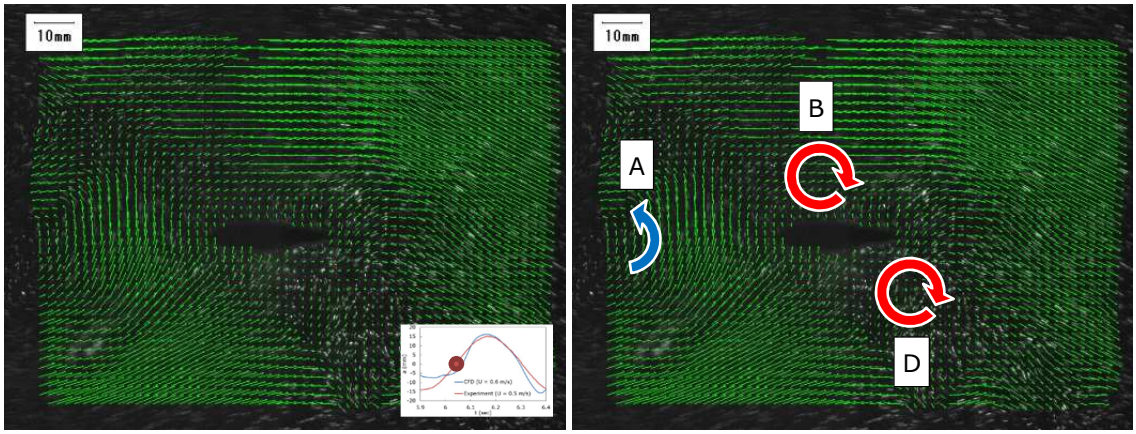

Figure 5.5 Flow field around the wing, (a) CFD result for a = 0 *mm*, (b) experimental result for a = 0 *mm*, (c) the CFD result with emphasized vortices and (d) the experimental result with emphasized vortices.

(a) (c)

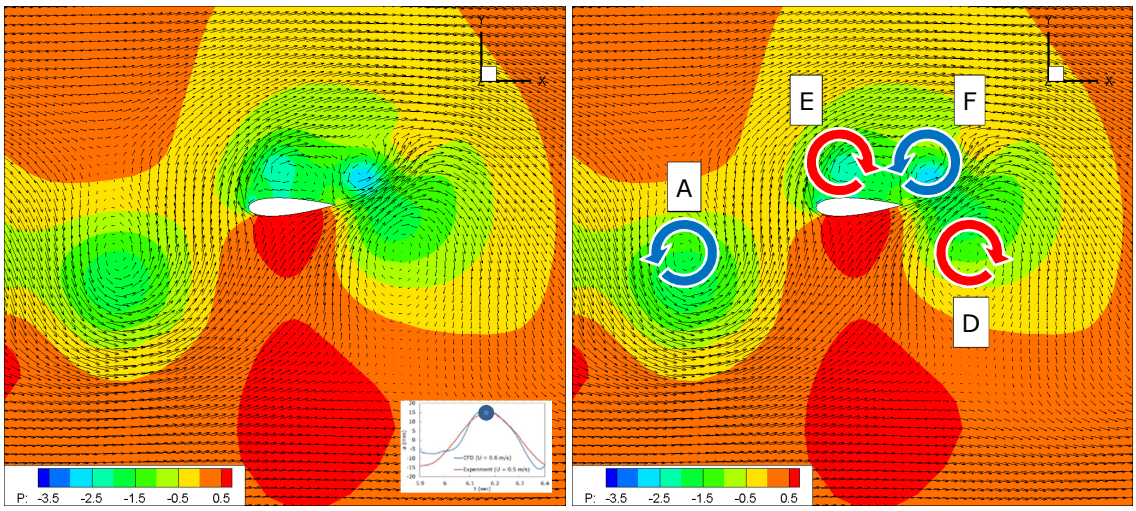

(b) (d)

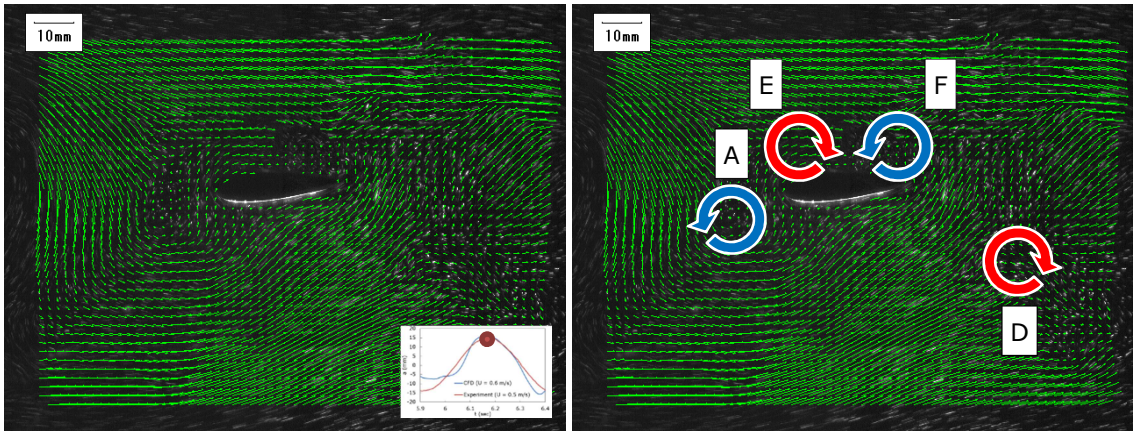

Figure 5.6 Flow field around the wing, (a) CFD result for a = 12 *mm*, and (b) experimental result for a = 12 *mm*, (c) the CFD result with emphasized vortices and (d) the experimental result with emphasized vortices.

(a) (c)

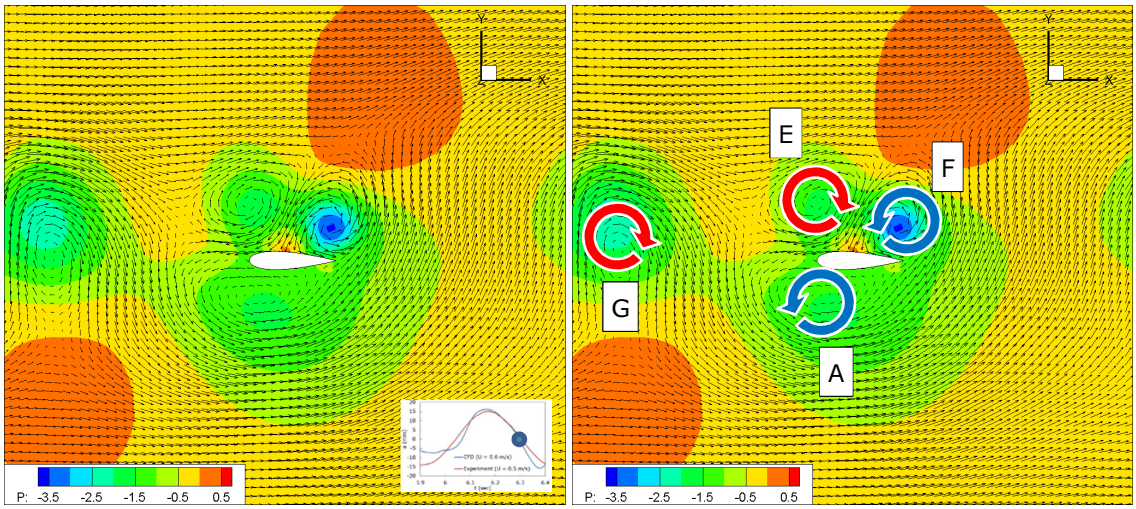

(b) (d)

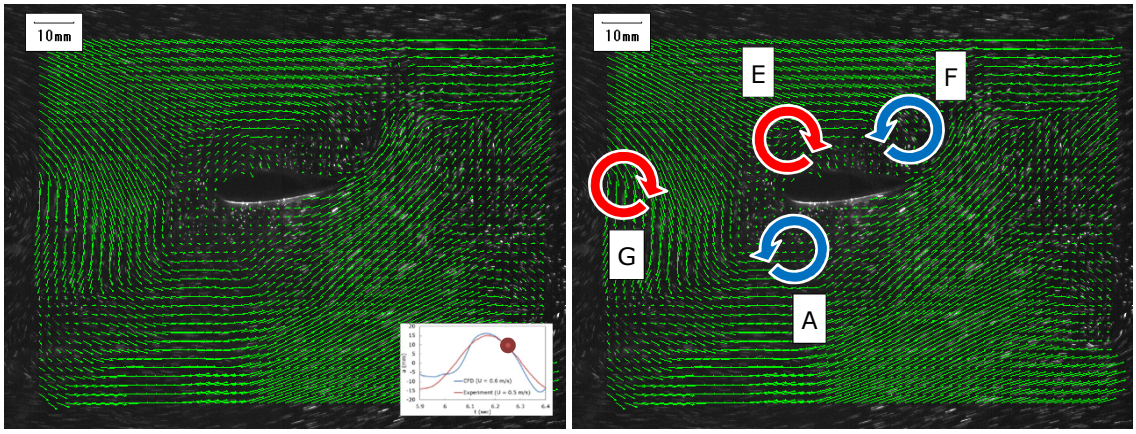

Figure 5.7 Flow field around the wing, (a) CFD result for a = 0 *mm*, and (b) experimental result for a = 10 *mm*, (c) the CFD result with emphasized vortices and (d) the experimental result with emphasized vortices.

CHAPTER 6

SUMMARY

We focused on dielectric elastomers (DEs) that are a new transducer technology to create a simple and efficient system for small-scale hydroelectricity, and proposed a power generating system for dielectric elastomers driven by Karman vortex street. This system extracts mechanical energy from fluid energy using the vibration of a wing which is set in the Karman vortex street in response to hydrodynamic force. The mechanical energy is transmitted to a DE generator through a shaft and subsequently converted into electrical energy.

In order to investigate the feasibility and the power generating performance of the proposed power generating system, an experimental model was fabricated and tested in a small circulating water channel. Furthermore, to show the characteristics of the present system, The motion of the wing and the flow fields around the wing were measured. Also two-dimensional CFD analysis was carried out for the small hydropower generation system proposed in this study to evaluate its generation performance in a wide range of parameters. The wing oscillations behind a circular cylinder which generates Karman vortices were simulated and the results were compared with the experimental data.

6.1 Conclusions

From this study, we obtained the following conclusions:

(1) The power generating system for the generators using dielectric elastomers with 8 *cm* diameter can be driven well by the Karman vortices in a water flow.

(2) We have to select the diameter of the cylinder and the size of the wing corresponding to the fluid velocity in order to obtain high efficiency of this system.

(3) The maximum energy efficiency is about 43% in the present system, when the water velocity is 0.4 *m/s*, the cylinder diameter is 48 *mm*, and the distance between the cylinder and the wing is 170 *mm*.

(4) The maximum average electric power of approximately 16 *mW* is verified with a generation efficiency of about 36%, when the span and chord length of the wing are 120 *mm* and 30 *mm*, respectively, the diameter of the cylinder is 60 *mm*, the distance between the cylinder and the wing is 170 *mm*, and the velocity of the water flow is 0.5 *m/s*.

(5) The wing vibration frequency agrees very well with the vortex shedding frequency.

(6) The wing oscillation amplitude becomes largest, i.e., the resonance amplitude, at a reduced velocity of approximately 5.

(7) Larger oscillation amplitude of the wing is obtained at a non-dimensional distance between the cylinder and the wing of approximately 2.67 because vortices which drive the wing are not fully developed near the cylinder owing to a dead water region.

(8) Two-dimensional flow analysis by CFD is capable of calculating the qualitative drive performance and reproducing the structure of the flow field obtained by experiments.

(9) By improving the accuracy of simulation (such as three-dimensional simulation), we can expect that the power generation performance of the system is predicted well by CFD.

We presented the characteristics of the power generating system for dielectric elastomers driven by Karman vortex street and estimated its electric power generation in this study. The proposed system consists of a simple structure and can be expected to be used at various locations in the future.

6.2 Future Work

We fabricated and tested the model based on the diaphragm-type DE generator having a diameter of 80 *mm*. In Section 3.3.3, scale-up of the proposed system is considered in order to produce larger power generation. Although the presumed results as shown in Figure 3.14 are obtained on the basis of the experimental results, the results have not been verified by experiments. Therefore, additional tests using the scaled-up model would be recommended to confirm the validity of the presumed results. Also experiments using actual DE generators are required.

The computational results show that the frequency of wing oscillation tends to be approximately 15% larger than the experimental results for the range of water speed tested. With regard to the wing oscillation amplitude, the CFD results show the different resonance point from the experimental results. These results are probably implicated in the conversion of the moment of inertial and the torsion spring constant to the simulation model and the two-dimensional flow assumption of the analysis. To validate the conversion process, additional comparison between computational and experimental results over a wide range of conditions (e.g. a diameter of a cylinder and distance from a cylinder to a wing) or three-dimensional simulations would be necessary and these are suggested as future works.

REFERENCES

1) REN21, “Renewables Global Futures Report”, 2013.
2) IEA-ETSAP, IRENA, “Hydropower”, Technology Brief E06, 2015.
3) REN21, “Renewables 2014 Global Status Report”, Paris, REN21, Secretariat.
4) IEA, “Key World Energy Statistics”, International Energy Agency, Paris, France, 76.
5) IJHD, “World Atlas & Industry Guide”, International Journal of Hydropower and Dams, Wallington, Surrey, UK, 2010, 405.
6) Egre D., Milewske J. C., “The diversity of hydropower projects”, Energy Policy, 30(14), 2002, 1225-1230.
7) Williamson S. J., Stark B. H., Booker J. D., “Low head pico hydro turbine selection using a multi-criteria analysis”, Renewable Energy, 61, 2014, 43-50.
8) Giosio D. R., Henderson A. D., Walker J. M. Brandner P. A., Sargison J. E., Gautam P., “Design and performance evaluation of a pump-as-turbine micro-hydro test facility with incorporated inlet flow control”, Renewable Energy 78, 2015, 1-6.
9) Laghari J. A., Mokhlis H., Bakar A. H. A., Mohammad H., “A comprehensive overview of new designs in the hydraulic, electrical equipments and controllers of mini hydro power plants making it cost effective technology”, Renewable and Sustainable Energy Reviews, 20, 2013, 279-293.
10) Shimokawa K., Furukawa A., Okuma K., Matsushita D., Watanabe S., “Experimental study on simplification of Darrieus-type hydro turbine with inlet nozzle for extra-low head hydropower utilization”, Renewable Energy, 41, 2012, 376-382.
11) Haidar A. M. A., Senan M. F. M., Noman A., Radman T., “Utilization of pico hydro generation in domestic and commercial loads”, Renewable and Sustainable Energy Reviews, 16, 2012, 518-524.

12) Pelrine R, Chiba S. “Review of artificial muscle approaches (invited)”, Proceedings of third international symposium on micromachine and human science. Nagoya, Japan. 1992. p. 1–9.
13) Osada Y, Taguchi T, “Soft Actuators which Drive Future Technologies –Recent R&D Activities Focused on Polymers and Biomaterials–”, CMC Publishing CO., LTD., 2010.
14) Asaka K, Okuzaki H, “Soft Actuators: Materials, Modeling, Applications, and Future Perspectives”, Springer, 2014.
15) Pelrine R, Kornbluh R, Joseph J, Heydt R, Pei Q, Chiba S, “High-field deformation of elastomeric dielectrics for actuators”, Materials Science and Engineering, C11, 2000, 89-100.
16) Chiba S, Pelrine R, Kornbluh R, Prahlad H, Stanford S, Eckerle J, “New opportunities in electric generation using electroactive polymer artificial muscle (EPAM)”, Journal of the Japan Institute of Energy, 86 (9), 2007 , 743-747.
17) Chiba S, Waki M, Kornbluh R, Pelrine R, “Extending applications of dielectric elastomer artificial muscle”, Proc. SPIE 6524, Electroactive Polymer Actuators and Devices (EAPAD), 652424, 2007, 1-5.
18) Chiba S, Waki M, Kornbluh R, Pelrine R, “Innovative power generation for energy harvesting using electroactive polymer artificial muscles”, Proc. SPIE 6927, Electroactive Polymer Actuators and Devices (EAPAD), 692715, 2008, 1-9.
19) Chiba S, Waki M, Wada T, Hirakawa Y, Masuda K, Ikoma T, “Consistent ocean wave energy harvesting using electroactive polymer (dielectric elastomer) artificial muscle generators”, Applied Energy, 104, 2013, 497-502.
20) Chiba S, Waki M, “Extending Applications of Dielectric Elastomer Artificial Muscles to Wireless Communication Systems”, Recent Advances in Wireless Communications and Networks, Prof. Jia-Chin Lin (Ed.), ISBN: 978-953-307-274-6, In Tech.
21) The Japan Society of Fluid Mechanics, Handbook of Hydrodynamics, 2nd ed., Maruzen, 1998.

22) Allen J. J., Smits A. J., “ENERGY HARVESTING ELL”, Journal of Fluids and Structures, 2001, 15, 629-640.
23) Zhu D., Beeby S., Tudor J., White N., Harris N., “A Novel Miniature Wing Generator for Wireless Sensing Applications”, Proc. The 9th IEEE Conference on Sensors 2010, Waikoloa, Hawaii, USA, November 1–4.
24) Akaydin H. D., Elvin N., Andreopoulos Y., “Wake of a cylinder: a paradigm for energy harvesting with piezoelectric materials”, Experiments in Fluids, 2010, 49, 291-304.
25) Wang D. A., Chiu C. Y., Pham H. T., “Electromagnetic energy harvesting from vibrations induced by Karman vortex street”, Mechatronics, 22, 2012, 746-756.
26) Wang D. A., Chao C. W., Chen J. H., “A miniature hydro-energy generator based on pressure fluctuation in Karman vortex street”, Journal of Intelligent Material Systems and Structures, 2012, 24(5), 612-626.
27) Nguyen H. D. T., Pham H. T., Wang D. A., “A miniature pneumatic energy generator using Karman vortex street”, J. Wing Eng. Ind. Aerodyn. 116, 2013, 40-48.
28) Demori M., Ferrari M., Ferrari V., Farise S., Poesio P., “Energy Harvesting from Von Karman Vortices in Airflow for Autonomous Sensors”, Procedia Engineering, 87, 2014, 775-778.
29) Hino T, “A 3D unstructured grid method for incompressible viscous flows”, Journal of the Society of Naval Architects of Japan, 182, 9-15, 1997.